Czech Technical University in Prague
Faculty of Nuclear Sciences and Physical Engineering

Physics Department

Branch: Experimental Nuclear and Particle Physics

Produkce mezonu upsilon v jádro-jaderných srážkách na experimentu STAR

Study of Upsilon meson production in heavy-ion collisions in the STAR experiment

RESEARCH PROJECT

Author: Bc. Jaroslav Štorek
Supervisor: Leszek Kosarzewski, BEng, Ph.D.
Year: 2019

ČESKÉ VYSOKÉ UČENÍ TECHNICKÉ V PRAZE
FAKULTA JADERNÁ A FYZIKÁLNĚ INŽENÝRSKÁ
PRAHA 1 - STARÉ MĚSTO, BŘEHOVÁ 7 - PSČ 115 19

Katedra: fyziky **Akademický rok:** 2018/2019

VÝZKUMNÝ ÚKOL

Student: Bc. Jaroslav Štorek

Studijní program: Aplikace přírodních věd

Obor: Experimentální jaderná a částicová fyzika

Vedoucí úkolu: Leszek Kosarzewski, BEng, Ph.D.

Mgr. Jaroslav Bielčík, Ph.D. - konzultant

Název úkolu (česky/anglicky): Produkce mezonu upsilon v jádro-jaderných srážkách na experimentu STAR / Study of Upsilon meson production in heavy-ion collisions in the STAR experiment

Pokyny pro vypracování:

1) Ultrarelativistické jádro-jaderné srážky
2) Interakce kvarkónií v kvark-gluonové plazmě
3) Přehled aktuálních měření mezonu upsilon na urychlovačích RHIC a LHC
4) Experiment STAR
5) Analýza experimentálních údajů

Součástí zadání výzkumného úkolu je jeho uložení na webové stránky katedry fyziky.

Literatura:

[1] A. Andronic, et al.: Heavy-flavour and quarkonium production in the LHC era: from proton–proton to heavy-ion collisions, Eur. Phys. J. C76 no.3, 107 (2016)
[2] R. Pasechnik and M. Sumbera: Phenomenological Review on Quark–Gluon Plasma: Concepts vs. Observations, Universe 3 no.1, 7 (2017)
[3] V. Khachatryan, et al.: Suppression of Upsilon(1S), Upsilon(2S) and Upsilon(3S) production in PbPb collisions at 2.76 TeV, Phys. Lett. B 770, 357-379 (2016)
[4] W. Zha, et al.: Systematic study of the experimental measurements on ratios of different Upsilon states, Phys. Rev. C 88, 067901 (2013)

Datum zadání: 22.10.2018 ....

Datum odevzdání: 28.06.2019 ***vedoucí katedry***

Acknowledgement

I would like to express my gratitude to Leszek Kosarzewski, BEng, Ph.D. and Mgr. Jaroslav Bielčík, Ph.D. for their valuable advices and comments to my research project.

Bc. Jaroslav Štorek

Název práce:

Produkce mezonu upsilon v jádro-jaderných srážkách na experimentu STAR

Autor: Bc. Jaroslav Štorek

Studijní program: Applications of Natural Sciences
Obor: Experimental Nuclear and Particle Physics
Druh práce: Research Project

Vedoucí práce: Leszek Kosarzewski, BEng, Ph.D.
Physics Department, Faculty of Nuclear Sciences and Physical Engineering, Czech Technical University in Prague

Konzultant: Mgr. Jaroslav Bielčík, Ph.D.
Physics Department, Faculty of Nuclear Sciences and Physical Engineering, Czech Technical University in Prague

Abstrakt: Produkce částic Υ slouží jako sonda pro zkoumání kvark-gluonového plazmatu. Na úvod jsou shrnuty základní modely jako Glauberův model a Bag model. Dále jsou uvedeny procesy ovliňující produkci Υ a přehled detektoru STAR. Po představení nejnovějších výsledků z kolaborací STAR a CMS následuje rekonstrukce částic Υ z dielektronového kanálu za použití dat nasbíraných při srážkách jader zlata na experimentu STAR při $\sqrt{s_{NN}} = 200$ v roce 2014. Uvedeny jsou závislosti spektra invariantních hmot na centralitě a rapiditě. Vypočtena byla závislost hrubého výtěžku Υ na rapiditě a závislost R_{AA} na N_{part}. Výsledný jaderný modifikační faktor je $R_{AA} = 0.29 \pm 0.06$ pro Υ(1S) and $R_{AA} = 0.25 \pm 0.10$ pro Υ(2S+3S) pro centralitu 0-60% a rapiditu $|y| < 0.5$

Klíčová slova: Srážky těžkých iontů, upsilon, kvark-gluonové plazma, experiment STAR

Title:

Study of Upsilon meson production in heavy-ion collisions in the STAR experiment

Author: Bc. Jaroslav Štorek

Abstract: Upsilon production studies provide a tool for investigating properties of quark-gluon plasma (QGP). Due to Debye-like screening, Upsilon suppression in QGP is expected. In the beginning of the research project, basics of heavy ion collisions, such as Glauber model and MIT Bag model, are described. Next, Upsilon production modification effects are discussed. After description of STAR detector, current Υ research at STAR and CMS experiments is overviewed. Finally, Υ signal reconstruction and nuclear modification factor R_{AA} computation from Au+Au $\sqrt{s_{NN}} = 200$ GeV collisions from Run 2014 is presented. Rapidity and centrality dependence of invariant mass spectra are showed and also dependence of Υ raw yield on rapidity and dependence of R_{AA} on number of participants are calculated. Results of R_{AA} are $R_{AA} = 0.29 \pm 0.06$ for Υ(1S) and $R_{AA} = 0.25 \pm 0.10$ for Υ(2S+3S) in 0-60% centrality interval and $|y| < 0.5$ rapidity interval.

Key words: Heavy-ion collisions, Upsilon, quark-gluon plasma, STAR experiment

Contents

Introduction

Desire to explore new things, and afterwards understand them, has always been characteristic for mankind and essential for survival. After thousands of years of discovering our world we have eventually approached a model which is satisfactorily describing matter around us and associated interactions, Standard Model of particle physics. In order to verify its validity, particle accelerators and colliders have been developed. These complex machines allow us to achieve energy densities comparable to those at the beginning of Universe. Now, heavy-ion physics has become a large branch of particle physics and it specializes in studies of heavy ion collisions, e.g. gold or lead ions. However, studies of relativistic heavy-ion collisions are not designed to search for new particles or verify the Standard Model, their goal is to investigate the properties of a hot and dense nuclear matter created in such collisions called quark-gluon plasma (QGP). It is a state of matter, where quarks and gluons are not bound in hadrons and can freely move within the medium, and is currently a field of intense studies at facilities like Large Hadron Collider or Relativistic Heavy Ion Collider. Understanding of QGP behavior allows us to model evolution of the Universe. One of the possibilities how to examine properties of QGP are studies of quarkonium production and related quarkonium melting.

In the research project, basics of nuclei collisions and quarkonium production are summarized. Also STAR detector and latest results of Υ studies in nuclei collisions are briefly discussed. Last part is dedicated to details of Υ signal reconstruction in Au+Au collisions at $\sqrt{s_{NN}} = 200$ GeV with the STAR experiment. Finally, short conclusion summarizes all the work within the scope of the research project.

Chapter 1

Relativistic Nuclear Collisions

There are two essential processes that may happen in a particle collision: elastic and inelastic scattering. In elastic scattering, only momentum transfer takes place and no new particles are created. Inelastic collision, unlike elastic, comprises creation of new particles and annihilation or change of structure of initial particles, which may no longer appear in the final state. To each types of collision we assign probability of its occurrence, elastic and inelastic cross section, σ_{el} and σ_{inel} respectively. Sum of these two is called total cross section σ_{tot}. It is worth noting, that inelastic cross section σ_{inel} dominates (Fig. 1.1). However, σ_{el} and σ_{inel} is being expressed only for nucleon-nucleon collision and in case of nuclei, elastic scattering is negligible.

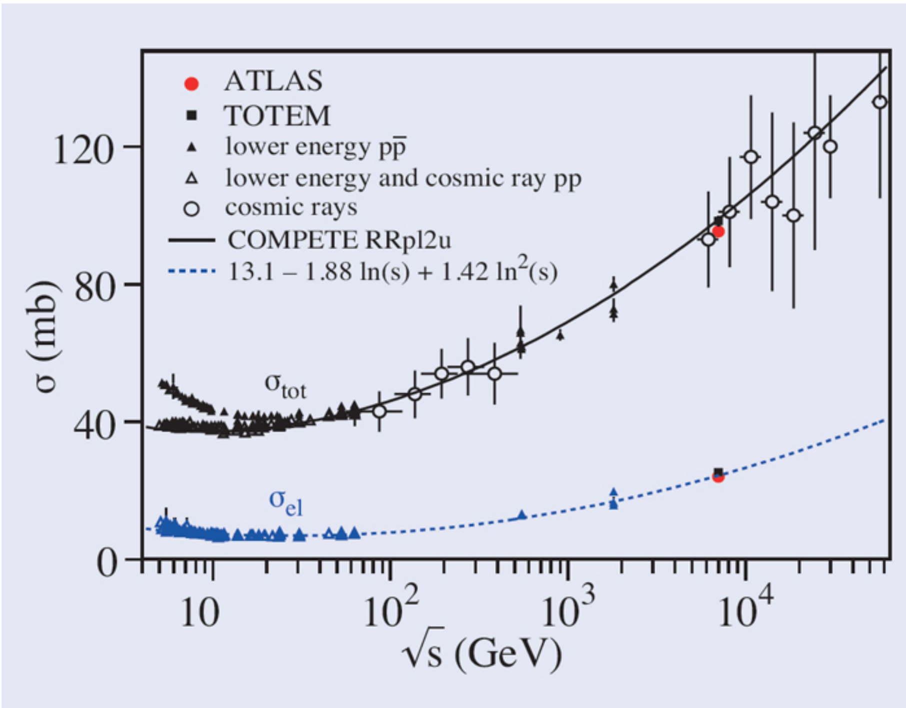

Figure 1.1: A graph illustrating dominance of inelastic scattering in p+p collisions at ATLAS [1].

1.1 Quark Confinement

Standard model describes the behavior of elementary particles interacting through three fundamental forces between each other. All the elementary particles and force carriers can be seen in Fig. 1.2. Protons and neutrons consist of quarks that interact by strong interaction carried by gluons. Overview of all interactions and their relative strength is summarized in Tab. 1.1. In this work we focus on studies of strong interaction between quarks and gluons. At low energies quarks behave according to Cornell potential [4]

$$V(r) = -\frac{a}{r} + br \quad , \tag{1.1}$$

where a, b are constants and r is radius of quarks. The linear term represents confinement of quarks in hadrons. On the other hand, at high energies quarks interact weakly similarly as for short distances. This phenomenon, where quarks are not tightly bound, is called asymptotic freedom.

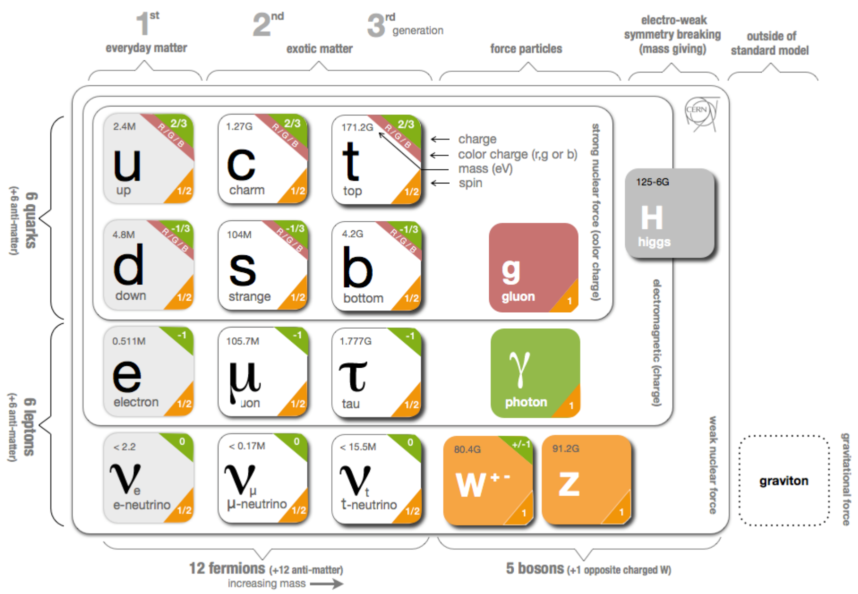

Figure 1.2: Standard model scheme [2].

Interaction	Force carrier	Rest mass [GeV/c^2]	Range [m]	Relative strength
strong	g	0	$\leq 10^{-15}$	1
electromagnetic	γ	0	∞	$\frac{1}{137}$
weak	$W^{\pm}$ a Z^0	80.41 a 91.18	10^{-18}	10^{-7}
gravitational	-	-	∞	10^{-39}

Table 1.1: Summary of four interactions [3].

1.2 Time Evolution of Nuclear Collision

Time evolution of nuclear collision performing inelastic scattering can be seen in the Fig. 1.3. Here, the z-axis represents the space coordinate along the beam direction, y-axis is time t. Collision happens at $t = 0$. Quark-gluon plasma (QGP), a state of deconfined quarks and gluons, is created shortly after the collision. The system cools with time and below a critical temperature for QGP formation T_c mixed phase of QGP and hadron gas is formed. At chemical freeze-out temperature T_{ch} all quarks and gluons finish hadronizing into hadrons and after cooling down below kinetic freeze-out temperature T_{fo} all interactions stop and momenta of outgoing hadrons are fixed.

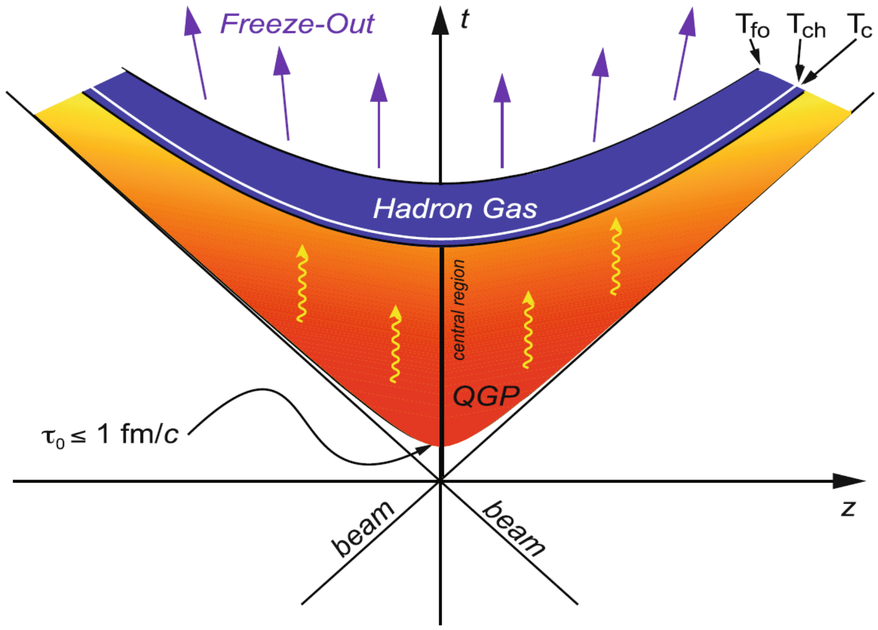

Figure 1.3: Diagram representing collision evolution in space (z) and time (t) coordinates [5].

1.3 Geometry of a Collision

Two colliding nuclei can hit each other in many ways depending on their mutual overlap. The distance between their centers is expressed by impact parameter b, which is a measure of collision centrality. In case of head-on collision, impact parameter equals zero and number of participants reaches its maximum (Fig. 1.4). In experiment, the impact parameter cannot be measured, only the number of charged particles in the final state. Charged particle multiplicity depends on number of participants N_{part} (soft interactions) and number of collisions N_{coll} (hard processes). Relation between impact parameter b, N_{coll} and N_{part} Monte Carlo Glauber model provides which uses Monte Carlo methods for nucleon distribution in nuclei. Here, Optical Glauber model will be introduced.

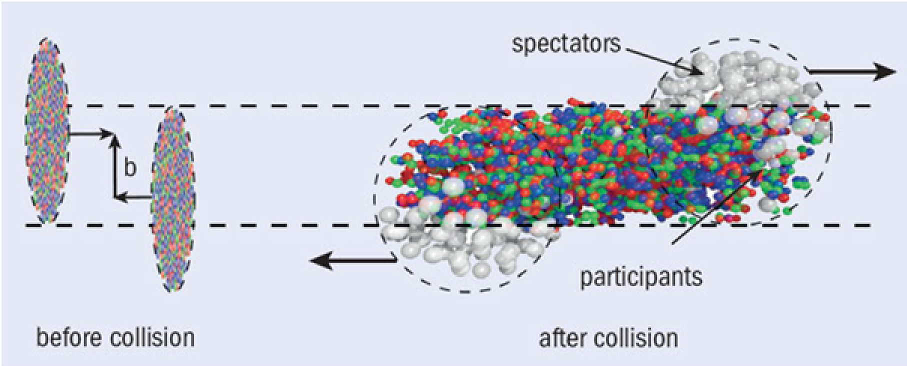

Figure 1.4: Illustration of impact parameter in a collision [6].

1.3.1 Optical Glauber Model

Optical Glauber model [7] is a geometrical model based on constant σ_{inel} for a given energy. First, nuclear thickness function $T_A(b')$ is calculated as an integral of density in longitudinal dimension $\rho_A(b', z)$ over longitudinal coordinate z

$$T_A(b') = \int \rho_A(b', z)dz \quad . \tag{1.2}$$

Let

$$\rho_A(z) = \begin{cases} \rho_0 & |z| \leq z_0 \\ 0 & \text{otherwise} \end{cases} \tag{1.3}$$

where $z_0 = \sqrt{R_A^2 - b'^2}$ denotes border of nuclei. From normalization that one nucleus has to contain A nucleons $\int T_A(b')d^2b' = A = \left(\frac{R_A}{r_0}\right)^3$ we obtain parameterization of density $\rho_0 = \frac{3}{4\pi r_0^3}$, where $r_0 \sim 1.2$ fm is a constant. These simple results are valid for sharp surface of nuclei only. Finer calculation can be done using Wood-Saxon density distribution of $\rho_A(z)$ with tail which plays a crucial role in peripheral collisions.

Probability $P_{AB}(b)$ of a nucleon-nucleon (NN) collision at impact parameter b is calculated as a product of (a) probability of finding a nucleon in a projectile nucleus A in a given volume element $d^2b_A dz_A$, (b) probability of finding a nucleon in a target nucleus B in the same volume and (c) the probability of an inelastic NN collision [7]:

$$\begin{aligned} P_{AB}(b) &= \int \frac{\rho_A(b_A, z_A)}{A} d^2b_A dz_A \cdot \frac{\rho_B(b_B, z_B)}{B} d^2b_B dz_B \cdot \sigma_{inel}\delta(b - b_A - b_B) \\ &= \frac{\sigma_{inel}}{AB} \int T_A(s)T_B(b-s)d^2s \\ &= \frac{\sigma_{inel}}{AB} T_{AB}(b) \end{aligned} \tag{1.4}$$

where we put for the probability of an inelastic NN collision inelastic cross section σ_{inel} times delta function, over which is integrated, and we also relabeled $b_A \to s$. Dividing by A or B results from probability normalization.

Because of AB being the maximum number of possible collisions, we can from last line of Eq. (1.4) identify $\sigma_{inel}T_{AB}(b)$ with number of NN collisions at impact parameter b, $N_{coll}(b) = \sigma_{inel}T_{AB}(b)$. While $T_{AB}(b)$ is a function of geometry and does not depend on energy, σ_{inel} does. The inelastic cross section grows from 32 mb at $\sqrt{s_{NN}} = 20$ GeV and 42 mb at $\sqrt{s_{NN}} = 200$ GeV to 60 mb at $\sqrt{s_{NN}} = 5.5$ TeV [7]. Thus $N_{coll}(b)$ is strongly energy dependent.

In the previous equation (1.4) we stated probability only for one collision. Now we write the probability for n inelastic collisions out of maximum number AB collisions [7]

$$P_{AB}(n,b) = \binom{AB}{n} P_{AB}(b)^n (1 - P_{AB}(b))^{AB-n} \tag{1.5}$$

where $\binom{AB}{n}$ is binomial coefficient. Assume more simple case and reduce nucleus B to one nucleon h. Sum over all possible number of collisions of nucleon h in nucleus A excluding the case of none collision leads to [7]:

$$\sum_{n=1}^{A} P_{hA}(n,b) = 1 - [1 - P_A(b)]^A \approx 1 - \exp(-\sigma_{inel}T_A(b)) \tag{1.6}$$

where we incorporated approximation $\sigma_{inel}T_A(b) \ll 1$. Here all possible collisions of one nucleon with nucleons in nucleus A are accounted for.

Finally we can express formula for number of participants in nucleus-nucleus collision. We substitute one nucleon in Eq. (1.6) with all nucleons in infinitesimally thin colliding cylinder – nuclear thickness function $T_B(b-s)$ – and also add the same part for the other nucleus [7]:

$$N_{part}(b) = \int d^2s \left[T_B(b-s)(1-\exp[-\sigma_{inel}T_A(s)]) + T_A(s)(1-\exp[-\sigma_{inel}T_B(b-s)])\right] \quad . \tag{1.7}$$

If $\sigma_{inel}T_A(s)$ and $\sigma_{inel}T_B(b-s)$ are large (central collision), exponentials may be neglected and formula reduces into [7]

$$N_{part}(b) = \int d^2s \left[T_A(s) + T_B(b-s)\right] \quad . \tag{1.8}$$

In Fig. 1.5 number of participants over impact parameter of various systems can be seen.

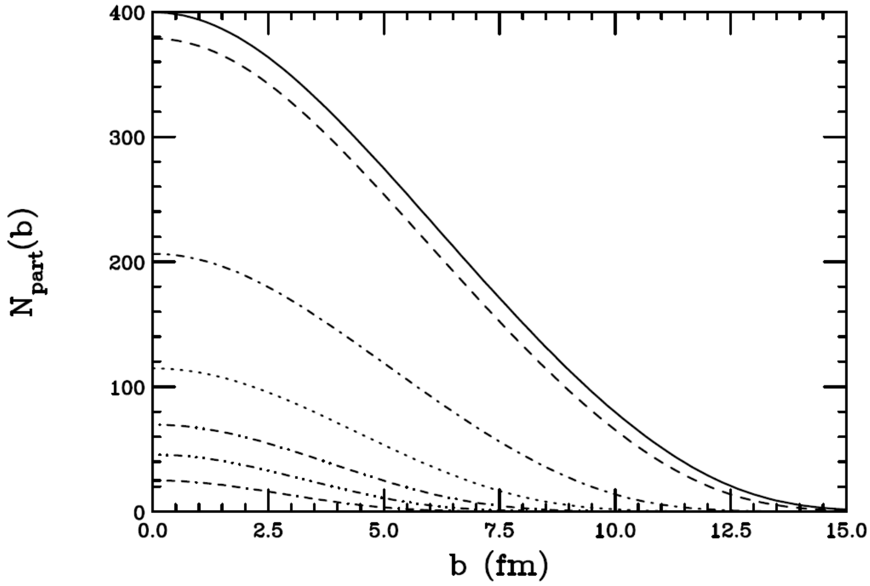

Figure 1.5: The number of nucleon participants N_{part} as a function of impact parameter b for O+O (dash-dash-dash-dotted), Si+Si (dot-dot-dotdashed), Ca+Ca (dot-dot-dash-dashed), Cu+Cu (dotted), I+I (dotdashed), Au+Au (dashed) and Pb+Pb (solid) collisions [7].

1.3.2 Centrality Determination

There are several ways how to determine centrality of a collision. One based on rapidity[1] loss, second based on transverse energy and last one depends on particle production. The two latter come out from the same principle.

Nucleon stopping in colliding nucleus is the main idea of rapidity loss measurement approach. Nucleon hits many nucleons in nucleus and the more collisions it undergoes, the more rapidity it looses. Some of them can be completely stopped. In order of accuracy, energy dependent cross section has to be taken into account because of energy changing multiple collisions of nucleon with other nucleons in nuclei.

The method based on energy measurement demands to distinguish transverse and longitudinal portion of nucleons energy. The produced particles in the collision gain energy especially in transverse direction E_T that is proportional to number of collided nucleons. If E_T is compared to energy of spectators (nucleons that did not interact), collision centrality can be estimated. Spectators' energy detectors are usually called zero degree calorimeters and are located at forward rapidity, close to beam rapidity.

Last centrality determination method is based on number of charged particles N_{ch} coming out of a collision. As Fig. 1.6 shows, the more produced charged particles the more central collision. Also can be seen that central collisions are very rare. Charged particle multiplicity determination is used at STAR.

[1]Defining a fourvector $P^{\mu} = (\frac{E}{c}, p_x, p_y, p_z)$, rapidity y equals $y = \frac{1}{2} \ln \left(\frac{E+p_z}{E-p_z}\right)^2$.

In next chapters central collisions refer usually to 0-10% of the most central collisions, semi-central collisions to 10-30% of the most central collisions and peripheral collisions to 30-60% of the most central collisions.

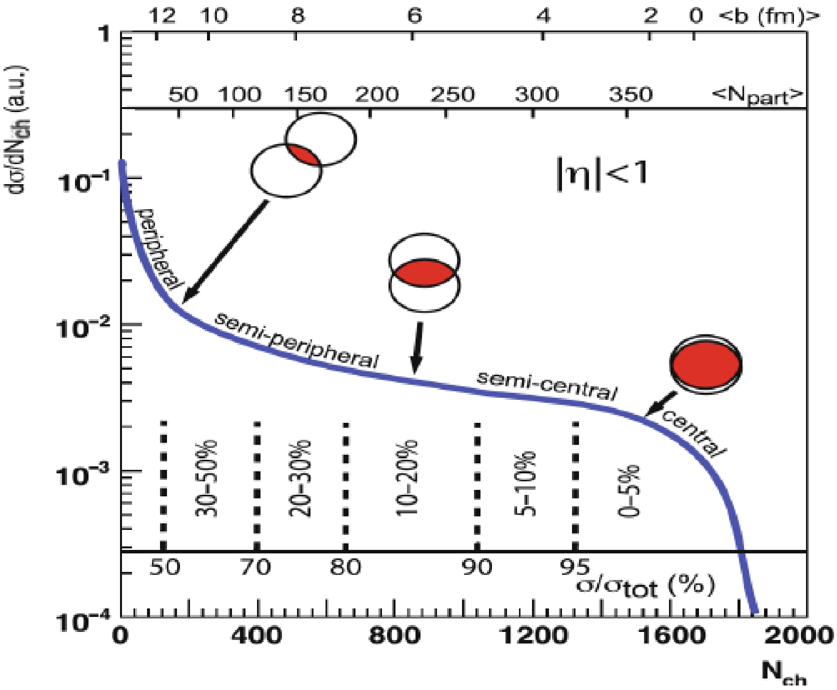

Figure 1.6: Illustrative graph of dependence of probability of type of a collision $\frac{d\sigma}{dN_{ch}}$, impact parameter b and number of participants N_{part} on number of charged particles N_{ch} [8].

1.4 MIT Bag Model

The Bag Model developed at MIT (Massachusetts Institute of Technology) describes a hadron as a bag confining non-interacting quarks in it [9]. It provides a good theoretical example which illustrates the possibility of a transition from hadron gas to quark-gluon plasma (QGP) state of matter, where quarks and gluons are not bound in hadrons and can freely move within the medium.

In this model quarks are held in a hadron by the bag pressure B. B points inward to the center of the hadron and compensates pressure of quarks caused by their kinetic motion.

Dependence of bag pressure B on number of particles N and radius of hadron R can be calculated from equality of inward and outward pressures. Considering massless fermions, one obtains [9]

$$B^{\frac{1}{4}} = \left(\frac{2.04N}{4\pi}\right)^{\frac{1}{4}} \frac{1}{R} \quad . \tag{1.9}$$

The value of the bag pressure $B^{\frac{1}{4}}$ for the confinement radius 0.8 fm and a 3 quark system in a baryon is equal $B^{\frac{1}{4}} = 206$ MeV [9]. This pressure overwhelms the external one and causes the quarks to expand and no longer be confined inside the bag. Thanks to this intuitive thermodynamic model it is easy to imagine, how this pressure excess could happen: either pressure of partons is too high (corresponds to high temperature) or too many partons try to fit in a very small area (large baryon number density).

1.4.1 High Temperature Regime

In terms of bag model, let noninteracting and massless quarks and gluons be in thermal equilibrium at large temperature T in volume V and assume an equal number of quarks and antiquarks, so baryon density is equal to 0. Sum of pressures of quarks, antiquarks and gluons leads to total pressure [9]

$$P = g_{total}\frac{\pi^2}{90}T^4 \quad , \tag{1.10}$$

where

$$g_{total} = g_g + \frac{7}{8}(g_q + g_{\bar{q}}) \quad . \tag{1.11}$$

Variables g_g, g_q and $g_{\bar{q}}$ are degeneracy numbers of gluons, quarks and antiquarks respectively. Additional contribution from the kinetic energy of the particles inversely proportional to the radius of the confined volume can be neglected due to consideration of deconfined volume. Taking into account degeneracy of 8 gluons and their 2 polarizations and for quarks and antiquarks three color charges, 2 spins and 2 flavors gives

$$P = 37\frac{\pi^2}{90}T^4 \quad . \tag{1.12}$$

The critical temperature T_c at which pressure P equals the bag pressure B for $B^{\frac{1}{4}} = 206$ MeV reaches

$$T_c = \left(\frac{90}{37\pi^2}\right)^{\frac{1}{4}} B^{\frac{1}{4}} \sim 144 \text{ MeV}. \tag{1.13}$$

Temperatures of the medium exceeding T_c cause breaking of the bag and quarks and gluons are deconfined in state of quark-gluon plasma.

1.4.2 High Baryon Density Regime

The bag pressure can be exceeded also by high baryon density in the bag. To avoid thermal contribution, $T = 0$ is assumed for this calculation. Pauli exclusion principle restricts filling the same states for fermions, therefore increasing the number of quarks results in occupation of different momentum states and increase of the pressure.

Pressure of relativistic degenerate quark gas P_q (without consideration of antiquarks and gluons) is [9]

$$P_q = \frac{g_q}{8\pi^2}\mu_q^4 \quad , \tag{1.14}$$

where g_q is quark degeneracy and μ_q is Fermi momentum. When pressure P_q reaches the bag pressure B value, Fermi momentum μ_q can be expressed as

$$\mu_q = \left(\frac{24\pi^2}{g_q}B\right)^{\frac{1}{4}} \quad . \tag{1.15}$$

Using the number density of the quark gas [9]

$$n_q = \frac{g_q}{6\pi^2}\mu_q^3 \tag{1.16}$$

we get critical baryon number density

$$n_{B,c} = \frac{1}{3}n_{q,c} = \frac{4}{3}\left(\frac{g_q}{24\pi^2}\right)^{\frac{1}{4}} B^{\frac{3}{4}} \quad . \tag{1.17}$$

Inserting values $g_q = 12$ and $B^{\frac{1}{4}} = 206$ MeV the critical baryon number density $n_{B,c}$ at which the compressed hadron matter becomes a quark-gluon plasma with a high baryon content at $T = 0$ equals $n_{B,c} = 0.72/\mathrm{fm}^3$ with Fermi momentum $\mu_{u,d} = 434$ MeV. Because these values are 5 times higher than that for normal nuclear matter, we can imagine this state of matter as compressed form of regular matter.

Untill now we discussed two extreme cases when one of the two components - either baryon density or temperature - equaled zero. In Fig. 1.7 the curve for other options is suggested also with experiments working on each particular area.

In Fig. 1.7 baryon density is expressed in terms of baryon chemical potential. It is expected to observe first order phase transition between quark-gluon plasma and hadron gas. Since first order phase transition is not observed along the temperature axis, it is great experimental challenge to find the critical point[2]. Purpose of RHIC (Relativistic Heavy Ion Collider) Beam Energy Scan is to investigate this area and determine the location of the critical point.

[2]Critical point is a location in a phase diagram where the boundary between the phases disappears.

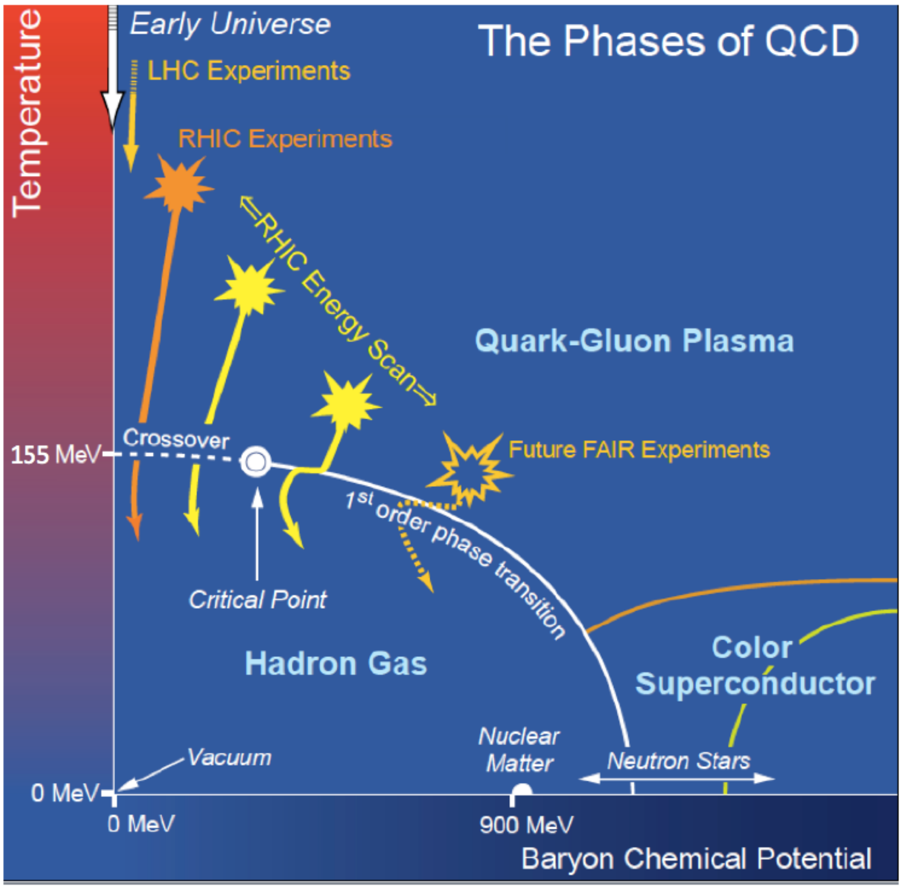

Figure 1.7: A sketch illustrating the experimental and theoretical exploration of the QCD phase diagram [10].

1.4.3 Lattice Gauge Theory

The Bag Model mentioned above serves especially as a guide and helps to illustrate reasons why transition into deconfined state of matter can happen. For better and more precise explanation, lattice gauge theory serves and gives prediction of deconfinement directly from first principle calculations.

For describing interactions between quarks and gluons, a theory called quantum chromodynamics (QCD) is used. QCD field can be divided into two branches: perturbative and nonperturbative. In perturbative QCD one obtains result only into a specific order of magnitude usually not higher than 4 because of complexity of calculations. Therefore perturbative QCD is sufficient only for short distance or high energy behavior of the system [9]. Moreover, to pass through divergent integrals, so called renormalization method has to be implemented. As a result of this procedure observable quantities such as mass and the coupling constant have to be redefined into unobservable bare quantities.

Among nonperturbative approaches lattice gauge theory counts. It is formulated on a discrete lattice of space-time coordinates. This finite spacing constrains divergent integrals from perturbative QCD and effectively applies a cut-off on them. Another advantage is applicability of path integral onto partition function in statistical mechanics allowing us to use Monte Carlo methods.

Lattice gauge theory gives physical predictions only if "scaling" behavior occurs. The number of lattice points and spacing between them has to be chosen so that the relationship between coupling constant and the scale of the lattice spacing a is in accordance with perturbative results [9]. Calculations are usually performed for various values of lattice spacing a and then extrapolated to $a \to 0$.

Chapter 2

Upsilons in Quark-Gluon Plasma

In relativistic nuclear collision there is energy of the order of GeV available for particle creation. In the creation process, conservation laws have to be fulfilled and with every particle, corresponding antiparticle is created. Particles then form bound states, especially with light quarks u and d. Creation of Upsilons Υ, which are $b\bar{b}$ bound states, is very rare because of their big rest mass (Tab. 2.1). Quarkonia ($q\bar{q}$) like J/Ψ and Υ interact with the QGP and dissociate at sufficently high temperature. Even though Υ mesons are even less abundant than J/Ψ, it is worth to study them because of less recombination and smaller cold nuclear matter effects [11].

Quarkonia are very rarely produced, but are formed in a very short time after a collision (< 1 fm/c). They are created even before QGP and are sensitive to its early-time dynamics [11]. Quarkonia strongly interact with the medium. Thanks to production modification, properties of QGP can be studied. In this chapter various production modifications are going to be introduced. Finally, a brief overview of commonly used models will be listed.

2.1 Color Screening

Lattice QCD calculations predict state of deconfined quarks and gluons (QGP) at high densities and temperatures [12]. In 1986, Matsui and Satz [13] proposed J/ψ suppression as a signature of formation of high temperature QGP. They came with an idea of color charge screening. Because of the high temperature in the medium, color charge that binds quarkonia together is screened by color charges of quarks and gluons in the medium. This causes the quarkonia to dissociate.

state	J/Ψ	χ_c(1P)	Ψ(2S)	Υ(1S)	χ_b(1P)	Υ(2S)	χ_b(2P)	Υ(3S)
mass [GeV/c^2]	3.07	3.53	3.68	9.46	9.99	10.02	10.26	10.36
radius [fm]	0.25	0.36	0.45	0.14	0.22	0.28	0.34	0.39

Table 2.1: Mass and radius for charmonia nad bottomonia [14].

The limit of the anomalous quarkonium dissociation can be expressed by Debye screening length r_D which is inversely proportional to temperature T, $r_D \sim 1/T$. When r_D becomes small, all states with radii larger than r_D ($r > r_D$) dissociate. Thanks to various radii of quarkonia (see Tab. 2.1), it is possible to indirectly measure temperature of the medium by observing a quarkonia sequential suppression [15]. Survival probability of Υ is illustrated in Fig. 2.1.

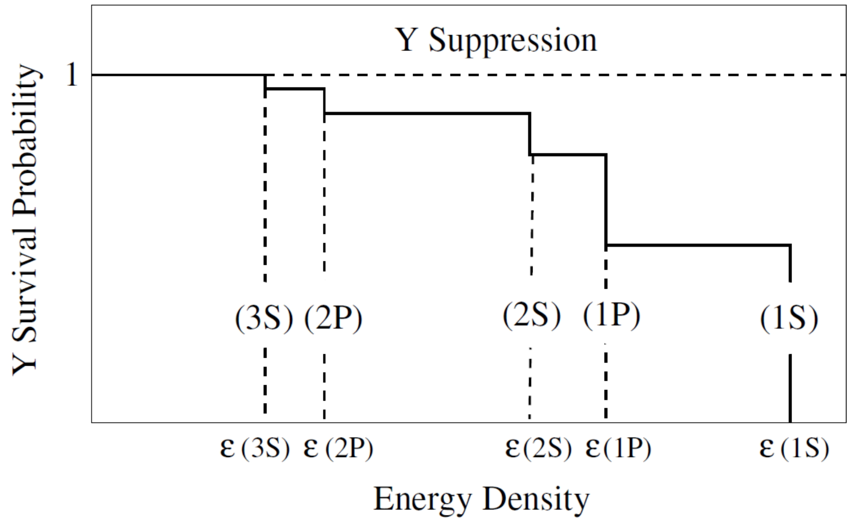

Figure 2.1: Schematic illustration of sequential quarkonium suppression for Υ [16].

2.2 Feed-down and Other Effects

In an experiment, where quarkonia are reconstructed, only inclusive quarkonia are observed and the ground state is usually the most abundant one. This is partially caused by contributions from deexcitation of other excited states, so called feed-down effect. Situation for Υ summarizes Tab. 2.2, in case of J/Ψ the contribution of direct J/Ψ is roughly around 40 % [5]. The deexcitation is realized by hadronic decays for S states and radiative ones for P states.

Direct Υ(1S)	$\sim$ 51 %
Υ(1S) from χ_b(1P) decay	$\sim$ 27 %
Υ(1S) from χ_b(2P) decay	$\sim$ 10 %
Υ(1S) from Υ(2S) decay	$\sim$ 11 %
Υ(1S) from Υ(3S) decay	$\sim$ 1 %

Table 2.2: Fractional contribution of Υ excited states to the ground state determined from $\sqrt{s_{NN}} = 39$ GeV proton collisions [17].

Not only suppression effects contribute to Υ production modification. There is also enhancement by recombination caused by coalescence of nearby b and $\bar{b}$, but this is expected to be very small for Υ [18]. Another possibility is that quarkonium escapes the area before the QGP creation and does not experience any effect of QGP, which is the so called leakage effect.

2.3 Cold Nuclear Matter Effects

In order to describe the observed suppression, Cold Nuclear Matter (CNM) effects have to be accounted for in the quarkonium suppression models. Assumption of too small system size for QGP creation in p+A or d+A collisions allows us to study CNM effects in that collisions. These CNM effects include shadowing, Cronin effect and nuclear absorption with comover interaction.

Modification of effective partonic luminosity in colliding nuclei with respect to that in proton collisions is one of the CNM effects. Distribution of partons in protons are described by parton distribution function (PDF). But partons in a single proton behave according to different dynamics than that in nuclei. The latter are influenced by partons from surrounding nucleons and their PDF is modified with respect to a free nucleon. For nuclear-modified PDF shortcut nPDF is used. Quantitatively the difference can be expressed by ratio R_i of nPDF to PDF [11]

$$R_i(x, Q^2) = \frac{\mathrm{nPDF}_i(x, Q^2)}{\mathrm{PDF}_i(x, Q^2)} \quad , \tag{2.1}$$

where index i denotes flavor of a parton. Parton distribution functions depend on Bjorken x, which is a fraction of the nucleon momentum carried by a parton, and square of four-momentum transfer Q^2.

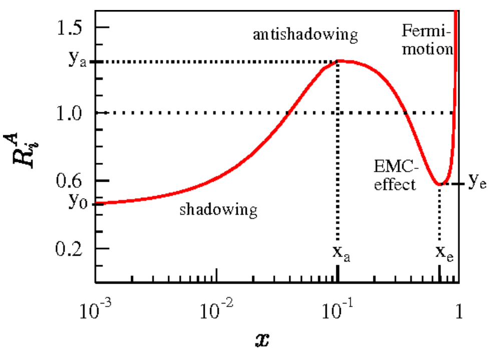

Figure 2.2: An illustration of R_i behavior dependent on Bjorken x [19].

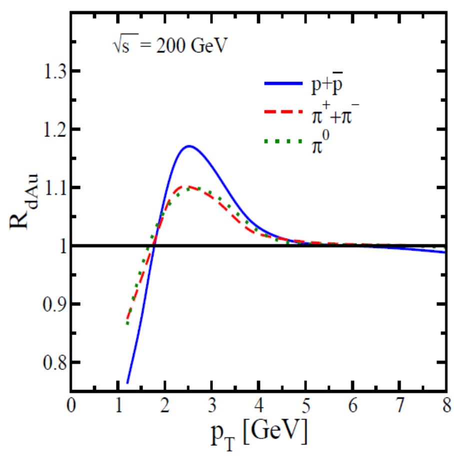

Figure 2.3: Modeled R_{dAu} dependence on p_T for protons and pions in midrapidity for RHIC [22].

In Fig. 2.2, an example shape of R_i can be seen. In region $x \lesssim 10^{-2}$, PDF dominates in (2.1) ($R_i < 1$). The effect is called shadowing and is related to phase-space saturation. Possible enhancement ($R_i > 1$) in area $10^{-2} \lesssim x \lesssim 10^{-1}$ refers to anti-shadowing. Last two effects comprise Fermi motion and yet unexplained EMC effect [20].

Cronin effect and nuclear absorption are also counted among CNM effects. Cronin effect describes enhancement of nuclear modification factor R_{pA} at high p_T [1] in p_T dependence by multiple subsequent scatterings of proton partons on partons of nuclei [21]. By this scattering partons get transverse momentum impulse and shift into higher p_T. Therefore with enhancement comes also suppression in lower p_T. Modeled R_{dAu} dependence on p_T can be seen in Fig. 2.3.

Nuclear absorption explains another addition to quarkonium production suppression. Here, quarkonia dissociate due to interaction with the nucleus [23].

Quarkonia can also interact with comoving hadrons, which is covered in the comover interaction model. Because of inelastic scattering with comoving hadrons, quarkonium dissociates which contributes to quarkonium suppression.

2.4 Nuclear Modification Factor

To quantify different effects of quarkonia production, nuclear modification factor R_{AB} is being introduced. Data from nuclei collisions are compared to the same data from proton collisions where creation of QGP is not expected. R_{AB} is a ratio of the yield of a particle of interest in AB collision N^{AB} with respect to pp collision N^{pp} scaled by the mean number of binary collisions $\langle N_{coll} \rangle$ and can be defined in dependence on chosen variable, usually transverse momentum p_T or number of participants N_{part}, as [24]

$$R_{AB}(p_T) = \frac{dN^{AB}/dp_T}{\langle N_{coll} \rangle dN^{pp}/dp_T} = \frac{dN^{AB}/dp_T}{T_{AB} d\sigma^{pp}/dp_T} \quad , \tag{2.2}$$

where σ^{pp} is cross section of charged particles in p+p collisions. Instead of using $\langle N_{coll} \rangle$, R_{AB} can be expressed in terms of nuclear overlap function T_{AB} from Glauber model and total inelastic cross section in pp collision σ^{pp}_{inel}, $T_{AB} = \langle N_{coll} \rangle / \sigma^{pp}_{inel}$. Notation of AB can represent two same nuclei (AA) or collision of nuclei and proton (pA) or deuteron (dA).

$R_{AB} > 1$ implies enhanced production in AB collision in comparison with pp collision and $R_{AB} < 1$ suppression of production.

[1] Defining a fourvector $P^\mu = (\frac{E}{c}, p_x, p_y, p_z)$, rapidity and transverse momentum equals $y = \frac{1}{2} \ln \left(\frac{E+p_z}{E-p_z}\right)^2$ and $p_T = \sqrt{p_x^2 + p_y^2}$ [7].

2.5 Quarkonium Production Models

To understand essential processes in quarkonium production, various models have been developed and compared to data. Most models incorporate both perturbative and non-perturbative aspects. Perturbative part is because of large momentum transfers in $q\bar{q}$ pair creation in hard scattering process and nonperturbative part is due to long distances over which $q\bar{q}$ state travels before quarkonium formation [11].

Most models treat production of $q\bar{q}$ pair and binding of quarkonia separately and differ especially in hadronisation stage. The Color-Evaporation Model (CEM), the Color-Singlet Model (CSM), and non-relativistic QCD will be presented.

In the Color-Evaporation model (CEM), the probability of quarkonium creation is directly proportional to probability of $q\bar{q}$ pair production in an invariant-mass region where hadronisation into a quarkonium is possible. That is between mass of two open-heavy-flavor hadrons and mass of two quarks [11]. This model also assumes that colors of the quarks are decorrelated compared to that at its production because of non-perturbative gluon emissions.

On the other hand, the Color-Singlet Model (CSM) presumes suppression of gluon emission according to power of $\alpha_s(m_q)$, therefore nor spin or color change is considered. Moreover, in CSM quarkonium can be formed only if the $q\bar{q}$ pair is created in a color-singlet state $(r\bar{r} + g\bar{g} + b\bar{b})/\sqrt{3}$. Quarkonium then inherits the same angular-momentum quantum numbers after $q\bar{q}$ [25]. Using correction of the order of α_s^4 and α_s^5 results in improved accuracy of CSM. In 1980's and 1990's both models, CEM and CSM, experienced considerable phenomenological success [25].

In 1995 a new approach of describing quarkonium production was proposed. Non-relativistic QCD (NRQCD) is effective field theory benefiting from both CEM an CSM. NRQCD utilizes factorization formula, whose one part comprises short-distance, perturbative effects involving momenta of order m_q, and the other part long-distance, nonperturbative effects. The nonperturbative factors in the NRQCD are integrated via long-distance matrix elements. In this formalism the so called color-octet process contributes – $q\bar{q}$ pair is produces in color-octet state and evolves non-perturbatively into a physical quarkonium [26]. Even though NRQCD is being developed longer than 20 years, complete proof of factorization of quarkonium production into perturbative $q\bar{q}$ pair creation and a non-perturbative bound state formation does not exist yet [11].

Chapter 3

Recent Measurements at LHC and RHIC

Upsilon production modifications are matter of current interest of many experimental and theoretical groups. The biggest conference, where physicist can share their new results from measurements or new theoretical approaches, Quark Matter, takes place regularly in one and half year with a few hundred physicists attending. This chapter contains a summary of latest Υ results from ALICE, ATLAS, CMS and STAR experiments. The ALICE, ATLAS and CMS experimental groups operate at Large Hadron Collider (LHC) at CERN in Europe, while STAR experimental group operates at BNL in State of New York.

3.1 Υ Results at ALICE

ALICE experiment is equipped by muon spectrometer, therefore ALICE focuses on the dimuon $\Upsilon \rightarrow \mu^+\mu^-$ decay channel of Upsilon. In center of mass frame the muon spectrometer covers forward rapidity $2.03 < y_{cms} < 3.53$ and backward rapidity $-4.46 < y_{cms} < -2.96$ [27]. Firstly, results from p+Pb collisions, where CNM effects can be studied, will be introduced, secondly Pb+Pb collisions.

In Fig. 3.1, nuclear modification factor Q_{pPb} dependence on mean number of collisions $\langle N_{coll}\rangle$ in p+Pb collisions for backward and forward rapidity at $\sqrt{s_{NN}} = 8.16$ TeV can be seen [27]. Nuclear modification factor is provisionally labeled as Q_{pPb} because of different treatment of systematic uncertainties and potential multiplicity biases connected to centrality estimation. $\langle N_{coll}\rangle$ has been extracted from Glauber model. $\langle N_{coll}\rangle$ corresponds to collision centrality similarly as number of participants N_{part}. In Fig. 3.1, no dependence of Q_{pPb} on $\langle N_{coll}\rangle$ is observed in studied range for forward nor backward rapidity. However, in forward rapidity the suppression is more significant.

In Fig. 3.2, nuclear modification factor R_{pPb} dependence on transverse momentum p_T in p+Pb collisions for backward and forward rapidity at $\sqrt{s_{NN}} = 8.16$ TeV is shown [27]. Data are compared to EPS09NLO + CEM model which comprises next-to-leading order nuclear parton distribution functions (nPDFs) and Color-Evaporation model discussed in previous chapter [28]. In both rapidity regions a bigger suppression in low p_T is observed. In forward rapidity, a good match between data and model is observed, while in backward rapidity model overestimates the data.

Next, nuclear modification factor R_{AA} at forward rapidity in Pb+Pb collisions has been studied at energies $\sqrt{s_{NN}} = 2.76$ TeV and $\sqrt{s_{NN}} = 5.02$ TeV [29]. In Fig. 3.3 is displayed R_{AA} dependence on number of participants $\langle N_{part} \rangle$, transverse momentum p_T and rapidity y. Data are compared to several models. In first transport model (TM1) the evolution of the thermal medium is based on a thermal-fireball expansion, while second transport model (TM2) incorporates a 2+1 dimensional version of the ideal hydrodynamic equations. Both transport models comprise both suppression and (re)generation mechanisms [30]. The potential for the $b\bar{b}$ pair in hydro-dynamical model is based on heavy-quark potential obtained from lattice QCD calculations in a hydro-dynamically evolving medium background [31].

In R_{AA} dependence on $\langle N_{part} \rangle$, a suppression towards more central collisions can be seen for both energies. In R_{AA} dependence on p_T or y, no significant dependence on both variables nor energy is observed. In all graphs in Fig. 3.3 models predict data reasonably well. However, in case of R_{AA} dependence on $\langle N_{part} \rangle$, TM1 model and hydro-dynamical model describes data better than TM2.

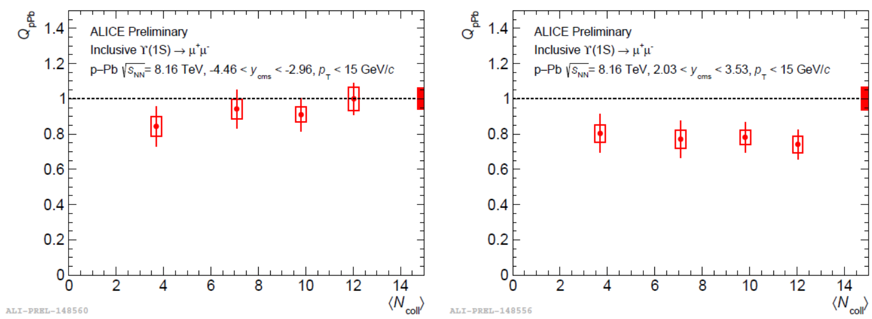

Figure 3.1: Dependence of $\Upsilon(1S)$ nuclear modification factor Q_{pPb} on centrality collision $\langle N_{coll} \rangle$ in backward (left) and forward (right) rapidity at $\sqrt{s_{NN}} = 8.16$ TeV [27].

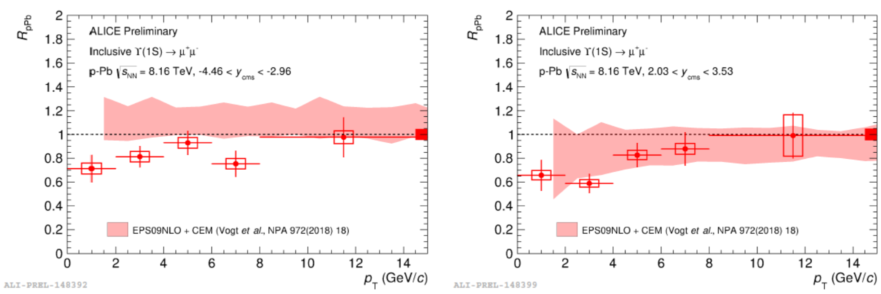

Figure 3.2: Dependence of $\Upsilon(1S)$ nuclear modification factor R_{pPb} on transverse momentum p_T in backward (left) and forward (right) rapidity at $\sqrt{s_{NN}} = 8.16$ TeV compared with EPS09NLO+CEM model [27].

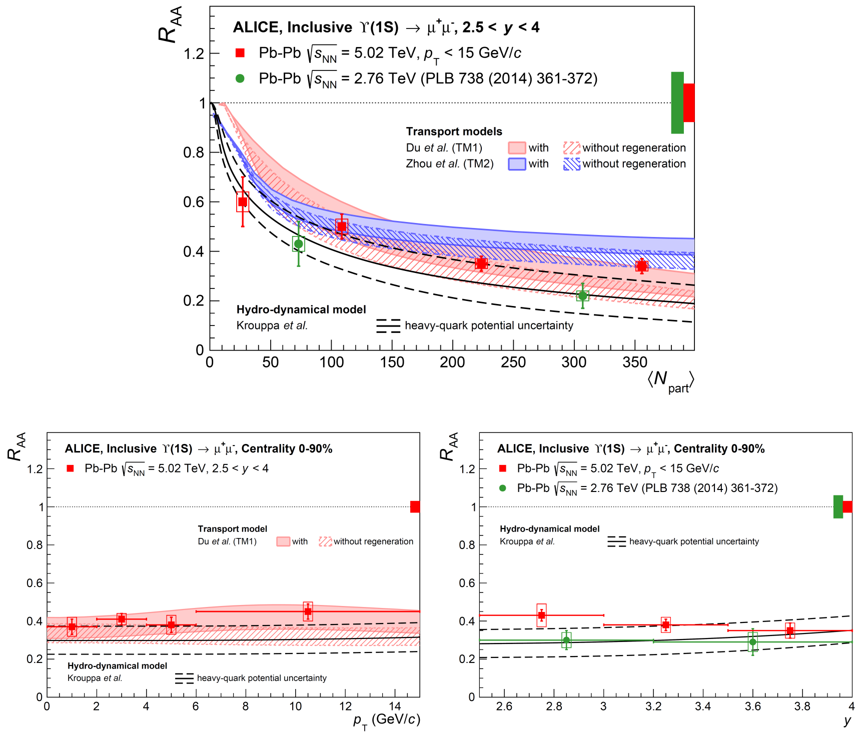

Figure 3.3: Dependence of Υ(1S) nuclear modification factor R_{AA} in Pb+Pb collisions on number of participants $\langle N_{part} \rangle$, transverse momentum p_T and rapidity y at energies $\sqrt{s_{NN}} = 2.76$ TeV and $\sqrt{s_{NN}} = 5.02$ TeV [29]. Data are compared with two transport models and one hydro-dynamical model.

3.2 Υ Results at ATLAS

In ATLAS experiment, Υ(1S) have been studied in p+Pb collisions at $\sqrt{s_{NN}} = 5.02$ TeV [32]. In Fig. 3.4, dependence of nuclear modification factor R_{pPb} on transverse momentum p_T (left) and rapidity y (right) can be seen.

In p_T dependence of R_{pPb}, Υ(1S) data are combined with J/ψ data. In low p_T, a suppression of both Υ(1S) and J/ψ can be observed, while above $p_T \gtrsim 10$ the data are consistent within uncertainties with unity, which points to negligible CNM effects in QGP studies at high p_T. Moreover, data agree reasonably well with EPS09 NLO model based on next-to-leading order nuclear parton distribution functions (nPDFs) [28].

In y dependence of R_{pPb}, data from ATLAS, LHCb and ALICE are compared. LHCb data confirm trend of bigger suppression in forward rapidities observed at ALICE, while ALTAS experiment investigates area of mid-rapidity. Data agree reasonably well within uncertainties. EPS09 NLO model successfully describes bigger suppression in forward rapidity.

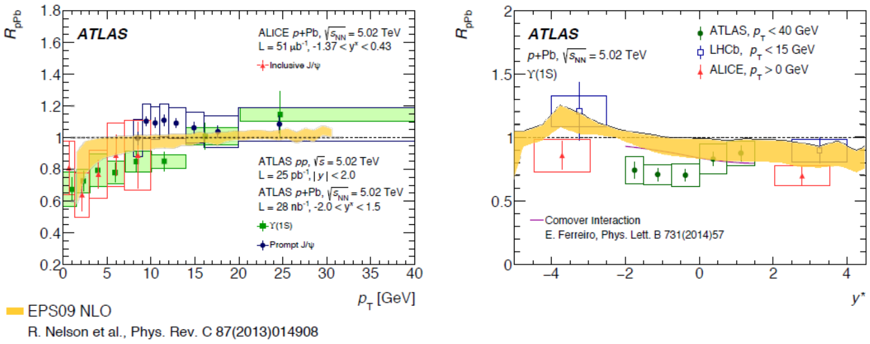

Figure 3.4: Dependence of nuclear modification factor R_{pPb} on transverse momentum p_T (left) and rapidity y (right) at $\sqrt{s_{NN}} = 5.02$ TeV for $\Upsilon(1S)$ and J/ψ [32]. Data from ATLAS, ALICE and LHCb experiments are combined for comparison.

3.3 Υ Results at CMS

In CMS experiment, Υ study has been performed via dimuon channel at energies $\sqrt{s_{NN}} = 2.76$ TeV and $\sqrt{s_{NN}} = 5.02$ TeV in lead-lead collisions. In Fig. 3.5 R_{AA} comparison of $\Upsilon(1S)$ for both energies can be seen, in Fig. 3.6 for $\Upsilon(2S)$ [33]. In $\Upsilon(1S)$ case, no significant difference between the data at the two energies is observed.

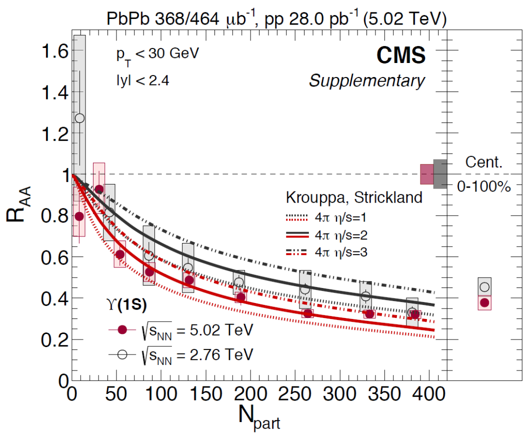

Figure 3.5: R_{AA} dependence on N_{part} for $\Upsilon(1S)$ at $\sqrt{s_{NN}} = 2.76$ TeV and $\sqrt{s_{NN}} = 5.02$ TeV energies with suggested model at CMS [33].

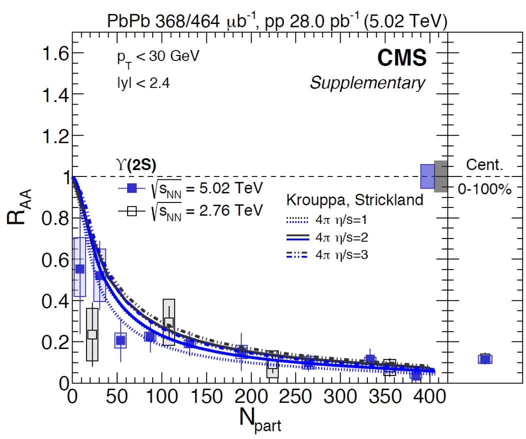

Figure 3.6: R_{AA} dependence on N_{part} for $\Upsilon(2S)$ at $\sqrt{s_{NN}} = 2.76$ TeV and $\sqrt{s_{NN}} = 5.02$ TeV energies with suggested model at CMS [33].

In both graphs, R_{AA} dependent on N_{part} is significantly suppressed in central collisions (high N_{part}). $\Upsilon(2S)$ is more suppressed than $\Upsilon(1S)$ which confirms idea of sequential melting with lower melting temperature for $\Upsilon(2S)$. Qualitatively $\Upsilon(1S)$ is suppressed approximately by a factor of 0.4 while $\Upsilon(2S)$ by a factor of 0.1 in central Pb+Pb collisions with respect to p+p collisions. Data in both graphs are within errors for $N_{\text{part}} > 100$ independent on collision energy per nucleon and show the same suppression. Peripheral collisions are less suppressed than the central ones with higher energy density. The measurement for energy $\sqrt{s_{NN}} = 5.02$ TeV experienced improvement in precision in comparison to $\sqrt{s_{NN}} = 2.76$ TeV measurement.

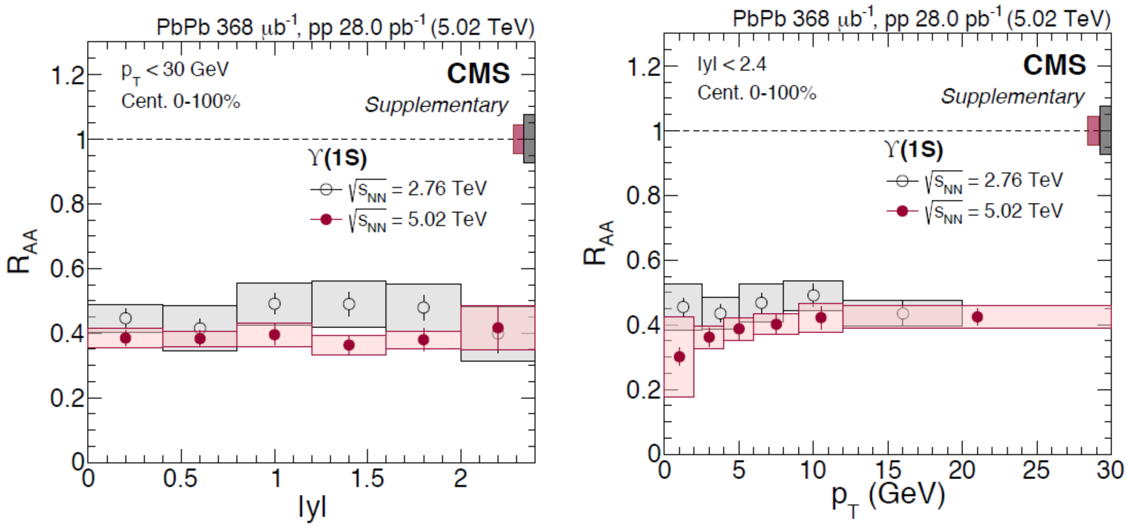

Figure 3.7: Rapidity and p_T dependence of R_{AA} for $\Upsilon(1S)$ at CMS [33].

In both graphs, three variations of Krouppa and Strickland model are showed. This model accompanies momentum-space anisotropy and no regeneration [33] and predicts initial temperature in collision around 550 MeV for $\sqrt{s_{NN}} = 2.76$ TeV and 640 MeV for $\sqrt{s_{NN}} = 5.02$ TeV. This model describes data very well in all centralities for $\Upsilon(1S)$, for $\Upsilon(2S)$ deviates for low centrality events.

Also rapidity y and p_T dependence of R_{AA} were studied in CMS collaboration (Fig. 3.7). Neither of them shows major fluctuations and both remain constant within error bars in studied $y = 0-2.5$ and $p_T = 0-30$ GeV intervals. $\Upsilon(2S)$ evinces again greater suppression than $\Upsilon(1S)$.

3.4 Υ Results at STAR

At STAR Au+Au collisions at $\sqrt{s_{NN}} = 200$ GeV energy per nucleon were studied in both dimuon and dielectron channels (Fig. 3.8) [34]. Data agree reasonably well. In Fig. 3.9 dependence of nuclear modification factor $R_{pA,AA}$ on number of participants N_{part} can be seen.

$\Upsilon(2S+3S)$ are reconstructed together because of lack of momentum resolution and data for $\Upsilon(3S)$ reconstruction and in central and semi-central collisions are more suppressed than $\Upsilon(1S)$ which is in agreement with expectations and CMS results from previous section. Suppression in central and semi-central collisions is for both $\Upsilon(1S)$ and $\Upsilon(2S+3S)$ approximately two times higher than that in peripheral case. For illustration of CNM effects, data from p+Au collisions are also shown. Combined $\Upsilon(1S+2S+3S)$ are in p+Au collisions two times less suppressed than in Au+Au.

Comparison of STAR and CMS $\Upsilon(1S)$ data for different energies and rapidities is shown in Fig. 3.10. Regardless of 10 times fold difference in center of mass energy per nucleon, the same suppression is observed. Possible explanation is stronger

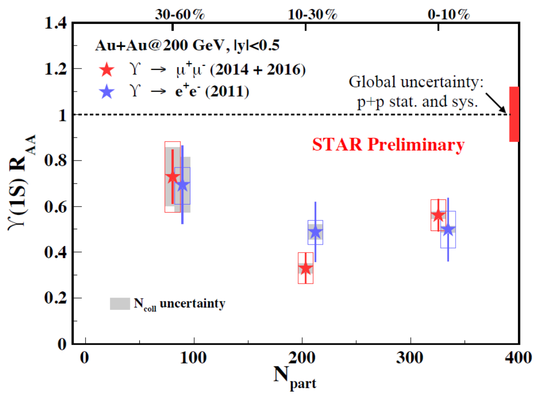

Figure 3.8: R_{AA} dependence on N_{part} for Υ(1S) at $\sqrt{s_{NN}} = 200$ GeV energy at STAR [34].

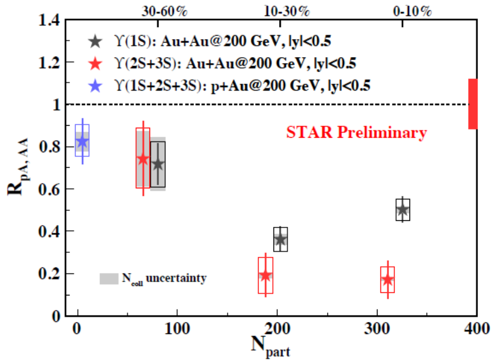

Figure 3.9: $R_{pA,AA}$ dependence on N_{part} for Υ(1S) (black stars), Υ(2S+3S) (red stars) and Υ(1S+2S+3S) (blue stars) at $\sqrt{s_{NN}} = 200$ GeV energy at STAR [34].

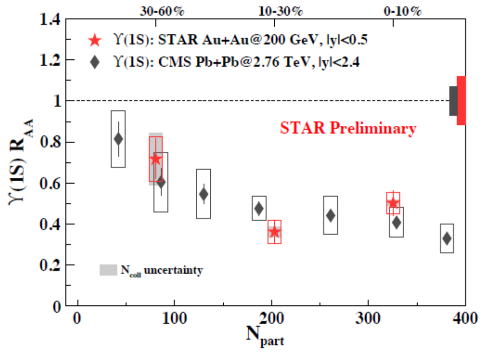

Figure 3.10: R_{AA} dependence on N_{part} for Υ(1S) at STAR and CMS [34].

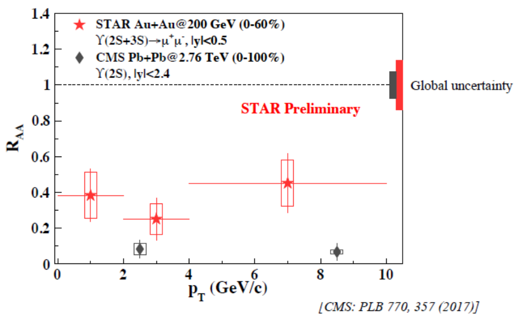

Figure 3.11: R_{AA} dependence on p_T for Υ(2S) (black diamonds) and Υ(2S+3S) (red stars) at CMS and STAR [34].

regeneration at LHC. No significant dependence of R_{AA} on p_T is observed for both STAR an CMS data (Fig. 3.11), however the suppression is greater for LHC energy.

Chapter 4

STAR Detector

In order to reach energy density high enough to create quark-gluon plasma in nuclei collisions, colliders such as Large Hadron Collider (LHC) or Relativistic Heavy Ion Collider (RHIC) are used.

RHIC (Fig. 4.1) is 3.8 km long and is located in Brookhaven National Laboratory (BNL) on Long Island in New York state [35]. Beam of particles is pre-accelerated in three stages before it gets into RHIC [36]. During 2000-2019 various systems in different energy ranges were collided: p+p within $\sqrt{s} = 62 - 510$ GeV collision energy range, Au+Au for $\sqrt{s_{\mathrm{N\,N}}} = 8 - 200$ GeV energies on a nucleon pair energies, U+U at $\sqrt{s_{\mathrm{N\,N}}} = 193$ GeV and others [37].

In the RHIC tunnel there are two beampipes which cross each other in 6 places called interaction regions. One of these interaction regions is in the center of the STAR detector. Schematic of the STAR experiment can be seen in Fig. 4.2. STAR with its weight 1,200 tons and size of a large house is designed to have large acceptance and to measure and identify particles in a large momentum range. To do so, various subdetectors are used, which are discussed in the text below.

Currently STAR is the only existing experiment at RHIC. However, sPHENIX detector is in development [38]. With its large acceptance $|\eta| < 1$ [1] and all the azimuthal angle will focus on probing quark-gluon plasma created in heavy ion collisions via jet and Upsilon studies. Resolution of sPHENIX will be good enough to distinguish all three Υ states Υ(1S), Υ(2S), Υ(3S) [38].

4.1 Time Projection Chamber (TPC)

Time projection chamber (TPC) is one of the most important detector in STAR. It's shape is cylindrical with 4 m diameter and length of 4.2 m [40]. TPC covers all the azimuthal angle and pseudorapidity up to $|\eta| < 1.8$ [2] and it's advantage lies in great performance in particle tracking, momentum and energy loss determination in

[1] $\eta = -\ln[\tan(\theta/2)]$, where θ is angle between particle's momentum and beam axis z [7].
[2] However, for a good quality track reconstruction only $|\eta| < 1$ range is usually used.

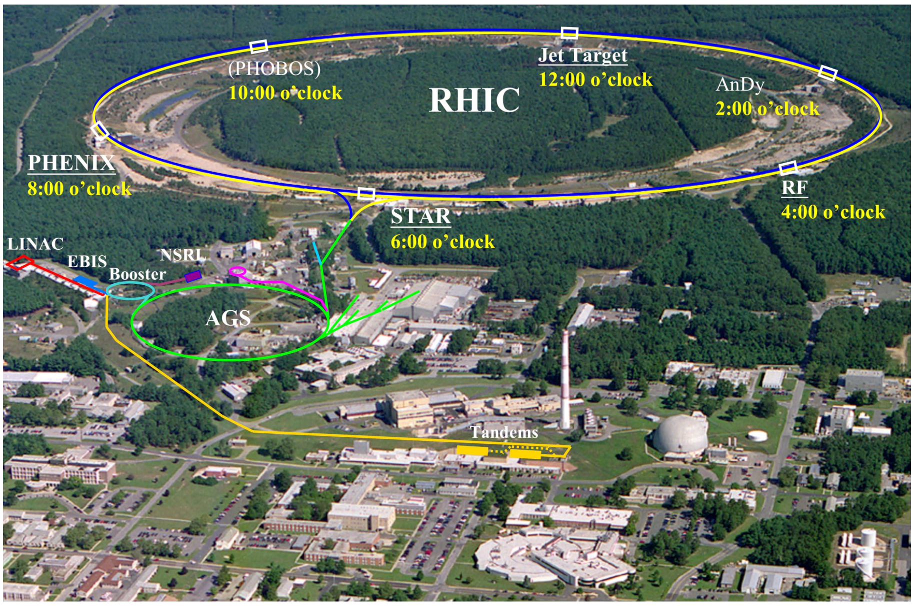

Figure 4.1: RHIC complex [36].

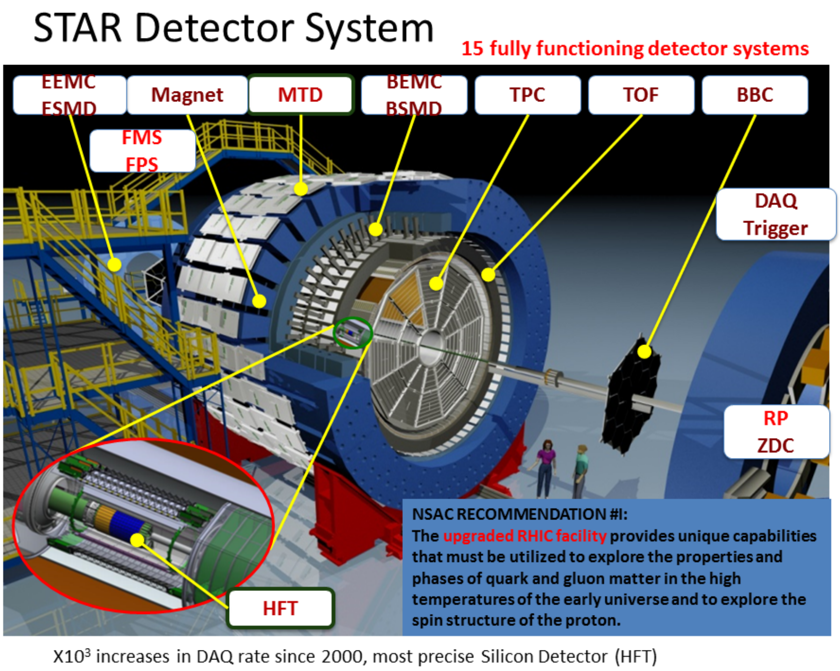

Figure 4.2: Scheme of STAR detector [39].

a high track density environment. A scheme is shown in Fig. 4.3.

TPC is placed in 0.5 T magnetic field and 135V/m electric field. P10 gas filling, which consist of argon form 90% and of methan from 10 %, gives the detector desired properties in drift speed of electrons created by gas ionization. Principally, signal is extracted from gathered electrons and ions created by ionization of the gas caused by passing charged particles. The electric field causes the freed electrons to drift to the Multi-Wire Proportional Chambers (MWPC) at endcaps, which allow 2D position measurement in the transverse plane. Every chamber consists of three wire

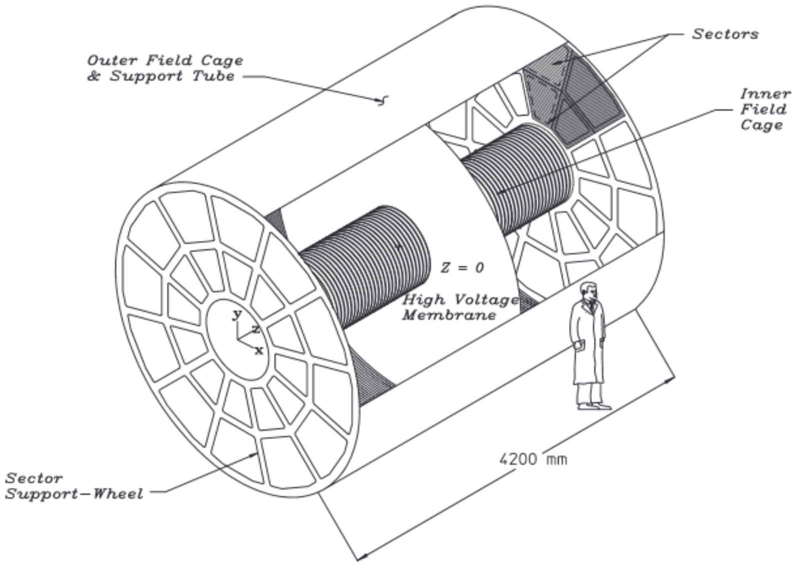

Figure 4.3: Scheme of TPC detector [40].

planes and a pad plane. Pad plane serves for readout while anode wires create the electric field with respect to grounded shield grid. Gating grid regulates electron flow [40]. Totally, there is 136,608 MWPC pads in all the TPC. The z coordinate is inferred from the drift time.

Momentum of a particle can be inferred from curvature of the track in magnetic field and energy loss dE/dx from integrated charge, which reaches the TPC pads. Theoretical reference for dE/dx is provided by modified Bethe-Bloch formula, so called Bichsel function [41]. Bichsel function has been developed empirically and reflects properties of the exact gas mixture used in STAR TPC. From TPC data particle identification is possible in range of particle momentum from 100 MeV/c to 1 GeV/c [40].

Position resolution depends on the drift distance and is roughly 1 cm. Transverse momentum resolution for π^- and anti-protons in the 0.25 T magnetic field can be seen in Fig. 4.4.

4.2 Barrel Electromagnetic Calorimeter (BEMC)

Barrel Electromagnetic Calorimeter (BEMC) is crucial for electron and photon energy determination. BEMC is cylindrical shell shape and surrounds TPC in all the azimuthal angle and pseudorapidity $|\eta| < 1$ in distance approximately 2.2 m from beam pipe (see Fig. 4.5). BEMC is made of 4800 calorimeter cells called towers divided into 120 modules and each of them points to interaction point. Every module with 40 towers is approximately 26 cm wide, 293 cm long (along the beam axis) and 39.5 cm high with one tower size $\sim 10 \times 10$ cm^2 at $\eta = 0$ which is increasing towards $\eta = 1$ [42]. Towers consist of lead and plastic scintillators layers

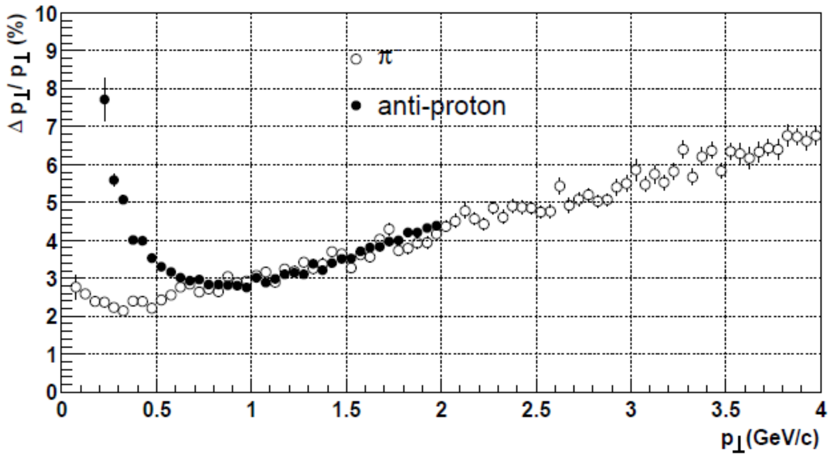

Figure 4.4: Transverse momentum resolution for π^- and anti-protons in the 0.25 T magnetic field [40].

where electromagnetic showers are converted into photons which are transported to photomultipliers located outside of magnetic field [42]. BEMC energy resolution is $\left(\frac{\sigma_E}{E}\right)^2 = \frac{0.14^2\text{GeV}}{E} + 0.015^2$ [42].

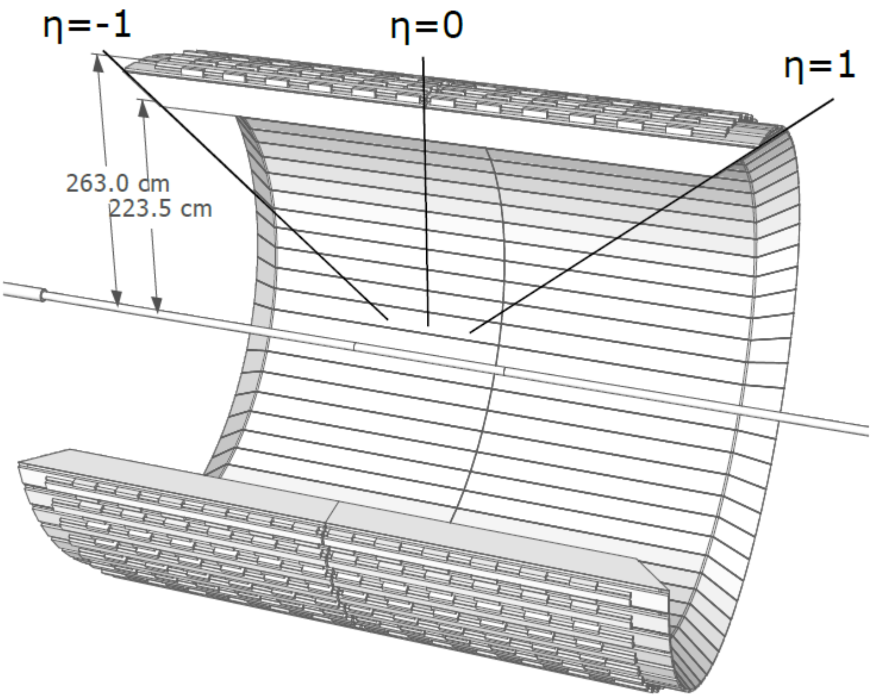

Figure 4.5: Scheme of BEMC detector [43].

BEMC also serves as a trigger for rare events. For example High Tower trigger identifies towers with energy above a given threshold. Because Υ decays into high energy electrons, data sample triggered by High Tower trigger has got a high probability of containing Upsilons and is useful for Υ analysis.

4.3 Muon Telescope Detector (MTD)

Muon Telescope Detector (MTD) is located beyond the BEMC and also outside of the STAR magnet [44]. In azimuthal angle MTD covers 45 % and in pseudorapidity $|\eta| < 0.5$. It is a gas detector filled with 95 % by freon and with 5 % by isobutan. Detection segments, Multi-gap Resistive Plate Chambers (MRPC), are divided in 5 chambers by glass layers [45]. Incoming charged particles create electron avalanches in these gas chambers. Scheme of the MTD and MRPC can be seen in Fig. 4.6.

MTD can be used as a dimuon trigger, therefore muons can be easily detected using MTD which is beneficial for Υ reconstruction in dimuon channel. Muons do not loose as much energy by bremsstrahlung as electrons and can be measured with better precision than electrons. However, MTD has got lower coverage in azimuthal angle and pseudorapidity than BEMC used for electron detection. Upsilon recostruction via dimuon channel serves as reliable check.

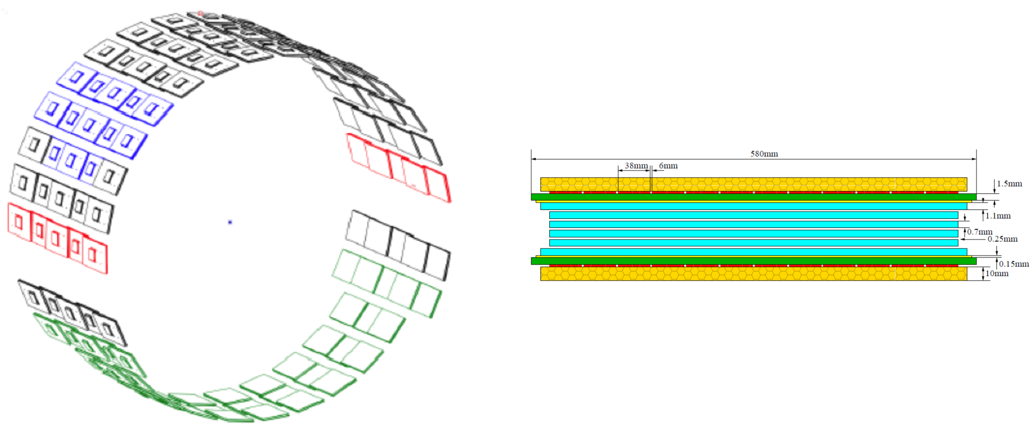

Figure 4.6: Scheme of Muon telescope detector (left) [46] and Multi-gap Resistive Plate Chambers (right) [45]

4.4 Vertex Position Detector (VPD)

Vertex Position Detector (VPD) is located very close to beam pipe at longitudinal distance $z = 5.6$ m from interaction point in both beam directions. VPD consists of lead and scintillator layers and signal is processed via photomultipliers. VPD serves as a trigger for Time of flight detector with a single detector resolution of 58 ps and is used for vertex position determination [47].

4.5 Beam-Beam Counter (BBC)

Beam-Beam Counter (BBC) is set of scintillators designed for luminosity measurement and triggering. BBC consist of two identical detectors located at pole tips of

STAR detector and covers full azimuthal angle and pseudorapidity $3.4 < |\eta| < 5.0$ [48]. BBC is also part of High Tower trigger used in Υ reconstruction.

4.6 Other Subdetectors

In this section subdetectors that do not contribute to Υ reconstruction are going to be briefly introduced. Detectors are listed in order of distance to the interaction point, from closest to furthest.

Heavy Flavor Tracker (HFT) was designed as a silicon based detector located closest to the interaction point. HFT covers all the azimuthal angle and pseudorapidity $|\eta| < 1$ [49]. Advantage of the HFT lies in very precise tracking of heavy flavor mesons and baryons which allowed direct reconstruction of their secondary vertices. HFT even exceeded it's designed resolution of distance of the closest approach of a track to the primary collision vertex which confirms success of HFT construction [50]. However, for particle reconstruction from electron channels HFT represented an obstacle, therefore was installed only for a few years.

On the endcaps of STAR detector, already mentioned BEMC is being supplemented by Endcap electromagnetic calorimeter (EEMC). EMC is contructed from lead and scintillator layers in a similar way as BEMC and covers the full azimuthal angle in $1 < \eta \leq 2$ region [51].

Time of Flight (TOF) detector is connected to VPD and measures traversing time of the particle. This gas filled detector based on Resistive Plate Chambers (RPC) is located 2.2 m from the interaction point and covers all the azimuthal angle and pseudorapidity $|\eta| < 1$. TOF contributes to resolution improvement in particle identification made by TPC [52].

Chapter 5

Data Analysis

As a part of this research project, Υ reconstruction from Au+Au collision at $\sqrt{s_{NN}} =$ 200 GeV energy via dielectron decay channel has been performed. Dataset collected in 2014 at STAR detector at RHIC has been studied. This dataset has got four times higher integrated luminosity $\mathcal{L}$ compared to dataset from 2011 presented in chapter 3. Greater luminosity can provide more precise results that will be an improvement over existing ones.

Data are stored in picoDST (reduced Data Storage Tree) format created by root4star utility. Root4star is modified ROOT [53] environment for data analysis in STAR experimental group. ROOT software based on C++ is widely used by particle physicists to process large amounts of data.

The recorded dataset is divided into two parts according to luminosity. From all the 129.8 M events 41 % falls into combined low and mid luminosity category, the rest to high luminosity one. Data were selected by Barrel High Tower trigger implemented using BEMC[1], which recorded only enough energetic events, and minimum bias trigger in VPD[2], which selected collisions happening in $|z| < 30$ cm. The integrated luminosity for this trigger is $\int \mathcal{L} dt = 4.5$ nb^{-1}. Basic information and trigger ID's are summarized in Tab. 5.1.

Collision type and energy	Au+Au at $\sqrt{s_{NN}} = 200$ GeV
Run year	2014
Trigger	BHT2*VPDMB-30
Trigger ID	450202, 450212
PicoDST production tag	P18ih
Number of events	129.8 M
Integrated luminosity	4.5 nb^{-1}

Table 5.1: Summary of the run 14 data set used for Υ studies.

[1] Barrel Electromagnetic Calorimeter
[2] Vertex Position Detector

5.1 Event Selection

As a first step, only well defined events close to interaction point are selected:

- all events that were distant more than 30 cm from the TPC center are rejected: $|v_z^{\mathrm{TPC}}| < 30$ cm cut is applied,
- only tracks that have point of primary vertex determined by VPD and that one determined by TPC closer than 4 cm; $|v_z^{\mathrm{TPC}} - v_z^{\mathrm{VPD}}| < 4$ cm.

After applying these selection criteria listed in Tab. 5.2, 126.5 M events remains. Both distributions can be seen in Fig. 5.1.

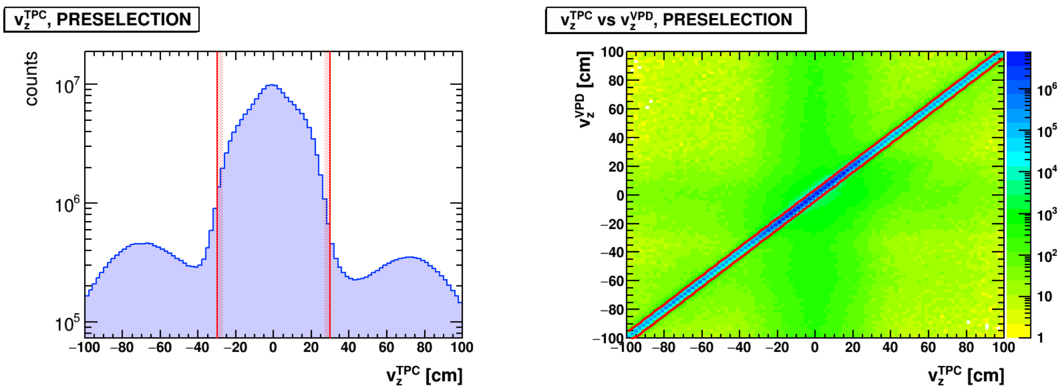

Figure 5.1: THIS ANALYSIS: Distributions of the z-coordinate of the primary vertex v_z^{TPC} (left) and v_z^{TPC} vs. v_z^{VPD} (right) with red lines denoting applied cuts.

5.2 Track Selection

In order to reconstruct Υ from dielectron channel (branching ratio B.R. $= (2.38 \pm 0.11)\%$ for Υ(1S) [54]), only highly energetic tracks of one electron and one positron that point into the same spatial point have to be selected. To do this, following cuts are performed.

Both tracks are primary tracks, i.e. come from primary vertex. The track has been obtained as a fit of at least 20 points detected by TPC which have to make at least 0.52 fraction of all possible points[3] for such track in order to ensure a good quality track. For dE/dx energy loss determination, at least 10 hit-points in TPC have been used, which ensured good dE/dx resolution. Furthermore, $|\eta| < 1$ cut is applied (Fig. 5.2a), to also ensure good quality track, and momentum of both tracks is chosen to be greater or equal 3.5 GeV/c to reduce low momentum background (Fig. 5.2b). Also distance of the closest approach of a track to primary vertex (DCA) has to be less or equal 3 cm to select only tracks coming from the primary vertex (Fig. 5.2c).

[3]The number of possible points is a hypothetical number of points that are created if a particle could produce all possible hits along its trajectory.

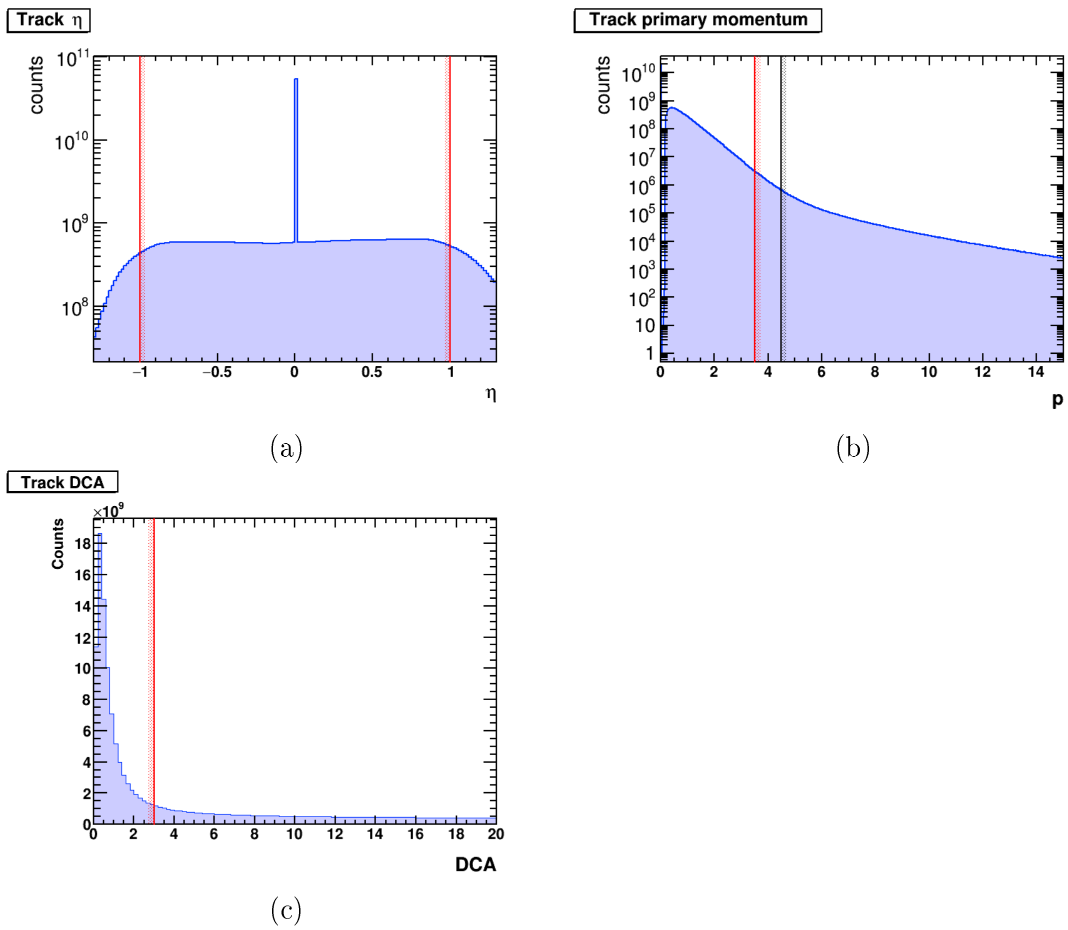

Figure 5.2: THIS ANALYSIS: Distributions of pseudorapidity η (5.2a), track primary momentum (5.2a) and DCA (5.2c) with red lines denoting applied cuts. The cut represented by black line applies for at least one electron. The peak at $\eta = 0$ corresponds to the non-primary tracks.

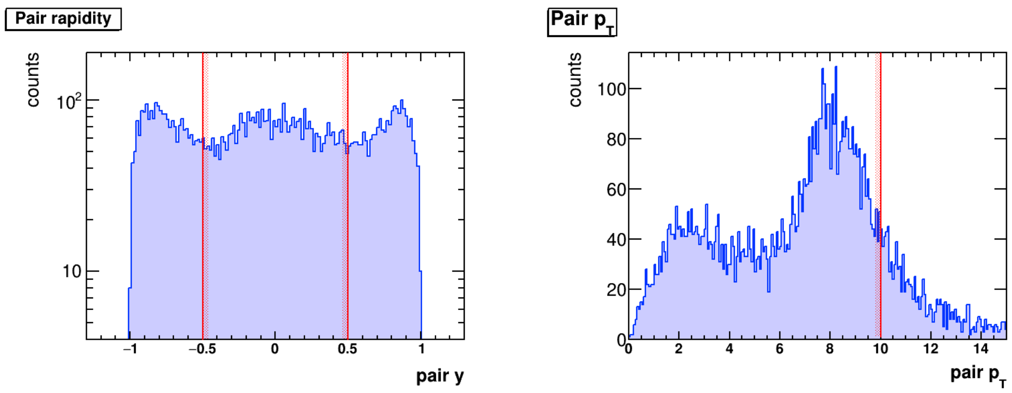

Figure 5.3: THIS ANALYSIS: Distributions of the pair rapidity (left) and pair p_T (right) with red lines denoting applied cuts.

Next, at least one electron has to have momentum greater than 4.5 GeV. To avoid any side effects on the edges of STAR detector, only pairs with rapidity in absolute value less or equal 0.5 are chosen. Finally, transverse momentum of electron pair has to be less or equal 10 GeV/c. All cuts are summarized in Tab. 5.2 and distributions are showed in Fig. 5.3 and 5.4.

Variable	Cut
Distance to TPC center	$\lvert v_z^{\text{TPC}}\rvert < 30$ cm
TPC and VPD determination difference	$\lvert v_z^{\text{TPC}} - v_z^{\text{VPD}}\rvert < 4$ cm
Primary track	$p \neq 0$
Number of TPC hits to realize a fit	$nHitsFit \geq 20$
Fraction of nHitsFit and all possible TPC hits of a track	$\frac{nHitsFit}{nHistMax} \geq 0.52$
Energy loss dE/dx points	$ndEdx \geq 10$
Pseudorapidity	$\lvert\eta\rvert \leq 1$
Momentum magnitude	$p \geq 3.5$ GeV
Distance of closest approach to primary vertex	DCA≤ 3 cm
Momentum magnitude of at least one electron	$p \geq 4.5$ GeV
Pair rapidity	$\lvert y\rvert \leq 0.5$
Pair p_T	$p_T \leq 10$ GeV

Table 5.2: Summary of the event and track cuts for Υ reconstruction.

5.3 Electron Identification Cuts

For electron identification, both TPC an BEMC detectors are used. Electron identification in TPC is based on dE/dx energy loss via $n\sigma_e$ variable which is defined

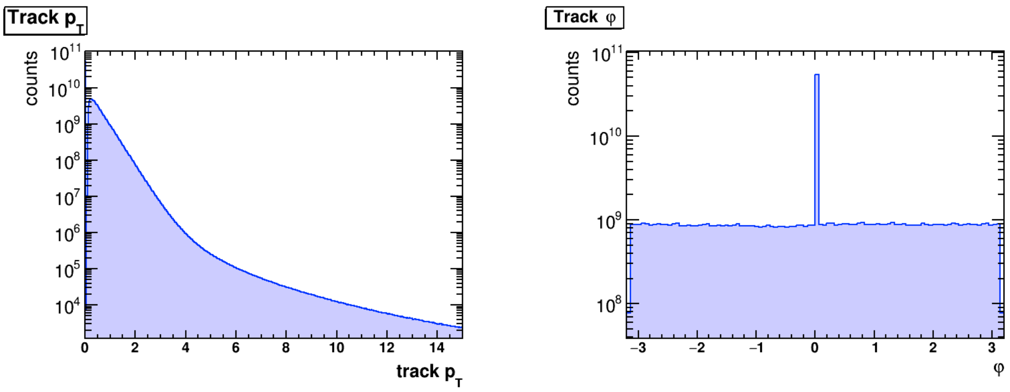

Figure 5.4: THIS ANALYSIS: Distributions of track p_T (left) and φ coordinate (right). The peak at $\varphi = 0$ corresponds to the non-primary tracks.

as

$$n\sigma_e = \ln \frac{dE/dx}{dE/dx|^e_{Bich}} / \sigma_{TPC} \quad , \tag{5.1}$$

where dE/dx is measured energy loss, $dE/dx|^e_{Bich}$ is expected energy loss for an electron predicted by Bichsel function and logarithm of these two is divided by dE/dx resolution of the TPC, σ_{TPC} [55]. For Υ reconstruction $-1.3 \leq n\sigma_e \leq 3$ cut is used which can be seen in Fig. 5.5a.

To ensure that energy deposited in BEMC really comes from electron track, a cut on distance R is applied. The distance is computed between track projection to BEMC layer and center of gravity of a cluster formed of at most three BEMC towers. Center of gravity has to be calculated because energy of the particle is spread among many towers. From all fired towers, three with the highest deposited energy make a cluster. Center of gravity of the cluster is calculated as energy weighed average of the tower positions in η and φ coordinates. R is then defined as

$$R = \sqrt{\Delta\eta^2 + \Delta\varphi^2} \quad , \tag{5.2}$$

where Δ denotes difference in position obtained from TPC and BEMC in corresponding coordinate. R has been restricted by applying $R \leq 0.026$ cut (Fig. 5.5b).

To ensure, that most energy of electrons is deposited in cluster of towers, $0.7 \leq \frac{E_{clu}}{p} \leq 1.4$ cut is performed. Because of small mass of electrons with respect to their momentum for energies on the order of GeV, most of the energy of an electron is its kinetic energy, $\frac{E_{clu}}{p} \sim 1$. Distribution and performed cut can be seen in Fig. 5.5c. All electron identification cuts are summarized in Tab. 5.3.

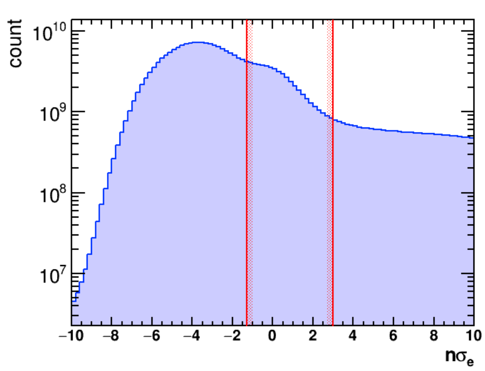

(a)

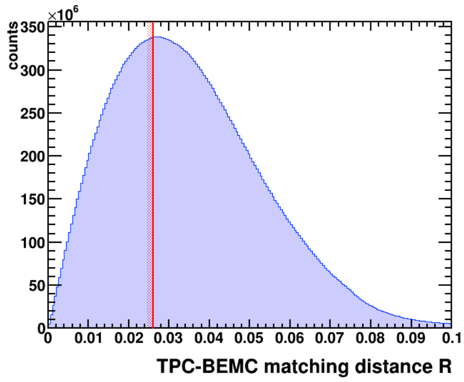

(b)

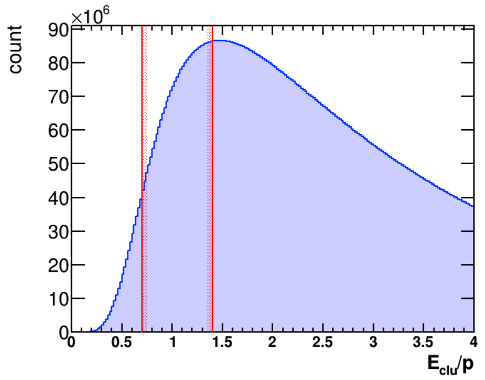

(c)

Figure 5.5: THIS ANALYSIS: Distributions of $n\sigma_e$ (5.5a), distance R (5.5b) and $\frac{E_{clu}}{p}$ (5.5c) with red lines denoting applied cuts.

Variable	Cut
TPC electron identification	$-1.3 \leq n\sigma_e \leq 3$
Distance between TPC and BEMC projected point	$R \leq 0.026$
Ratio of energy and momentum	$0.7 \leq \frac{E_{clu}}{p} \leq 1.4$

Table 5.3: Summary of the electron identification cuts for Υ reconstruction.

5.4 Υ Signal Reconstruction

In order to reconstruct Υ via dielectron channel, invariant mass spectrum of observed e^+e^- has to be obtained and the signal extracted using statistical methods. Invariant mass is calculated according to equation

$$m_{e^+e^-} = \sqrt{(E_1 + E_2)^2 - (\vec{p_1} + \vec{p_2})^2} \quad , \tag{5.3}$$

where E_1, E_2 and $\vec{p_1}$, $\vec{p_2}$ are energies and momenta of daughter electrons. Significantly visible peak around mass 9.46 GeV/c^2 corresponds to the signal of Υ(1S).

Observed signal is combination of e^- and e^+ coming from Upsilons and from other processes which are considered as background. The background is made of combinatorial and correlated parts. Combinatorial part is formed from completely uncorrelated e^-e^+ pairs coming from random processes. Estimate of shape of the combinatorial background is done by constructing like-sign electron e^-e^- and positron e^+e^+ pairs because they can not originate from Υ. Concurrent method is mixing events where e^-e^+ pair is formed from electron and positron coming from totally different event. However, event mixing is not performed in this analysis.

Correlated background covers processes where e^- and e^+ is created in a decay of other particles. Such processes are Drell-Yan process ($q\bar{q} \rightarrow e^-e^+$) and decays of B mesons, i.e. $b\bar{b} \rightarrow B\bar{B} \rightarrow e^-e^+ + X$, while the former is much less significant [56]. Correlated background was simulated by PYTHIA and GEANT simulation tools using STAR-HF-Tune parameters [57]. PHYTHIA is Monte Carlo generator for event simulation while GEANT reproduces particle interaction with detector. In this analysis, $B\bar{B}$ decays has been taken into account only for initial individual b quarks with p_T greater than 5 GeV/c and Drell-Yan processes has been neglected [58].

5.4.1 Signal Extraction

Raw yield of Υ states is obtained from fitting unlike-sign mass spectrum. Signal of different Υ states is modeled by Crystal-Ball functions [59]. Signal line shape deviates from Breit-Wigner distribution because of detector momentum resolution and bremsstrahlung of electrons. Crystall-Ball function constitutes of a Gaussian core with a power-law low-end tail. Parameters of the Crystal-Ball function are determined from simulation [58].

Fitting process is done via a dedicated fitting libraries RooFit, which is a part of ROOT framework. To avoid background contribution, following procedure has been performed.

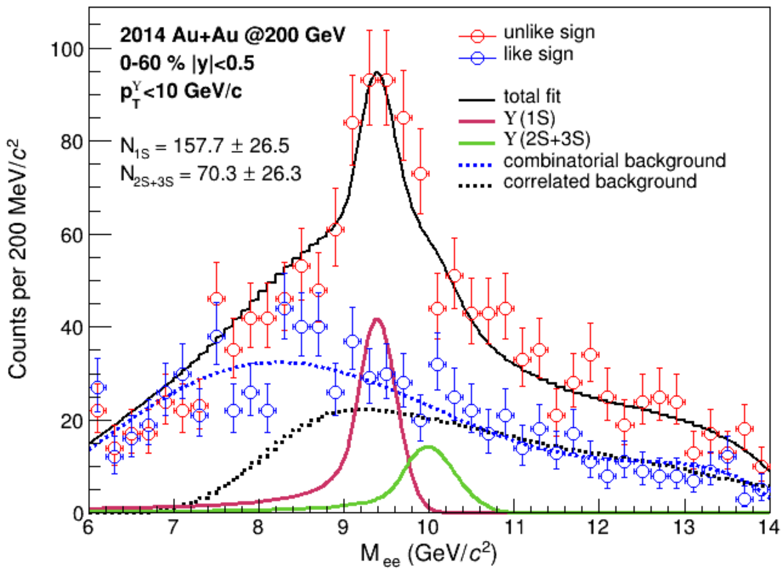

Figure 5.6: THIS ANALYSIS: Reconstructed Υ signal in 0-60% centrality class.

Firstly, uncorrelated background is fitted with a third-order Chebychev polynomial in range (6;14) GeV/c^2 and is fixed for purpose of subsequent fits. Correlated background is incorporated in form of a histogram obtained directly from simulation to avoid bias. Next, Υ line shapes are set and Υ(2S) to Υ(3S) ratio is set to world wide value (0.689:0.311)[4] [58]. Finally, unlike-sign spectrum fit is performed in (6;14) GeV range incorporating both backgrounds and Υ(1S) and Υ(2S+3S) shapes. Υ(1S) and Υ(2S+3S) signals are extracted from the fit.

Four centrality intervals have been studied 0-60%, 0-10%, 10-30%, 30-60% in $|y| < 0.5$ rapidity and also signal outside of $|y| < 0.5$ rapidity in 0-60% centrality interval have been calculated. Results for 0-60% centrality class are shown in Fig. 5.6 and for 0-10%, 10-30%, 30-60% centrality classes in Fig. 5.7 for $|y| < 0.5$. Signal for forward and backward rapidity is displayed in Fig. 5.8. Fig. 5.9 shows signal dependence on rapidity. Lower yield at side rapidities is observed as expected. In case of Υ(2S+3S) the result is consistent with no signal.

5.5 Efficiencies

Signal from raw yield has to be corrected for detector acceptance and reconstruction efficiency. To determine them, method called embedding is used. In embedding, real and simulated data are combined and subsequently analyzed the same way as the

[4] If the world average ratio (0.682:0.318) [60] is used, effect on total yield is of the order of 1% in Υ(1S) case and 0.1% in Υ(2S+3S) case.

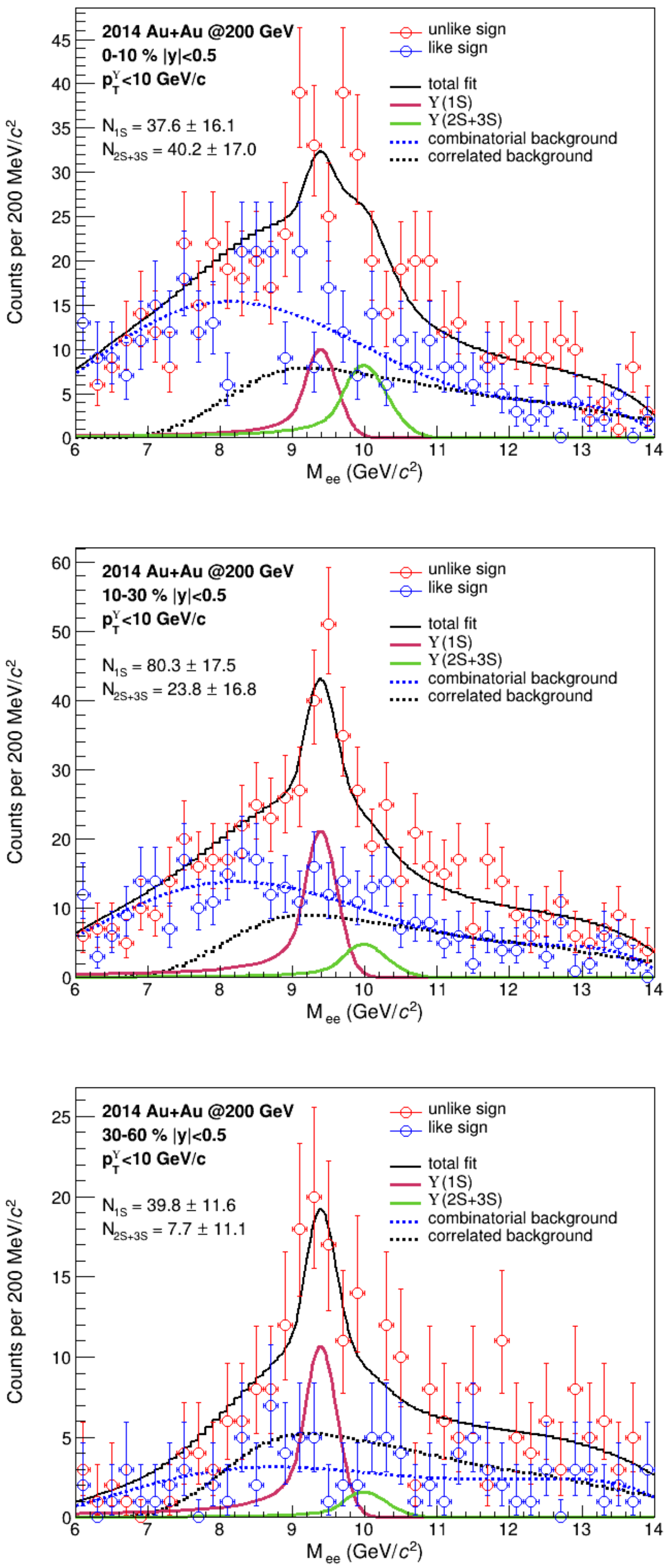

Figure 5.7: THIS ANALYSIS: Reconstructed Υ signal in 0-10%, 10-30%, 30-60% centrality classes.

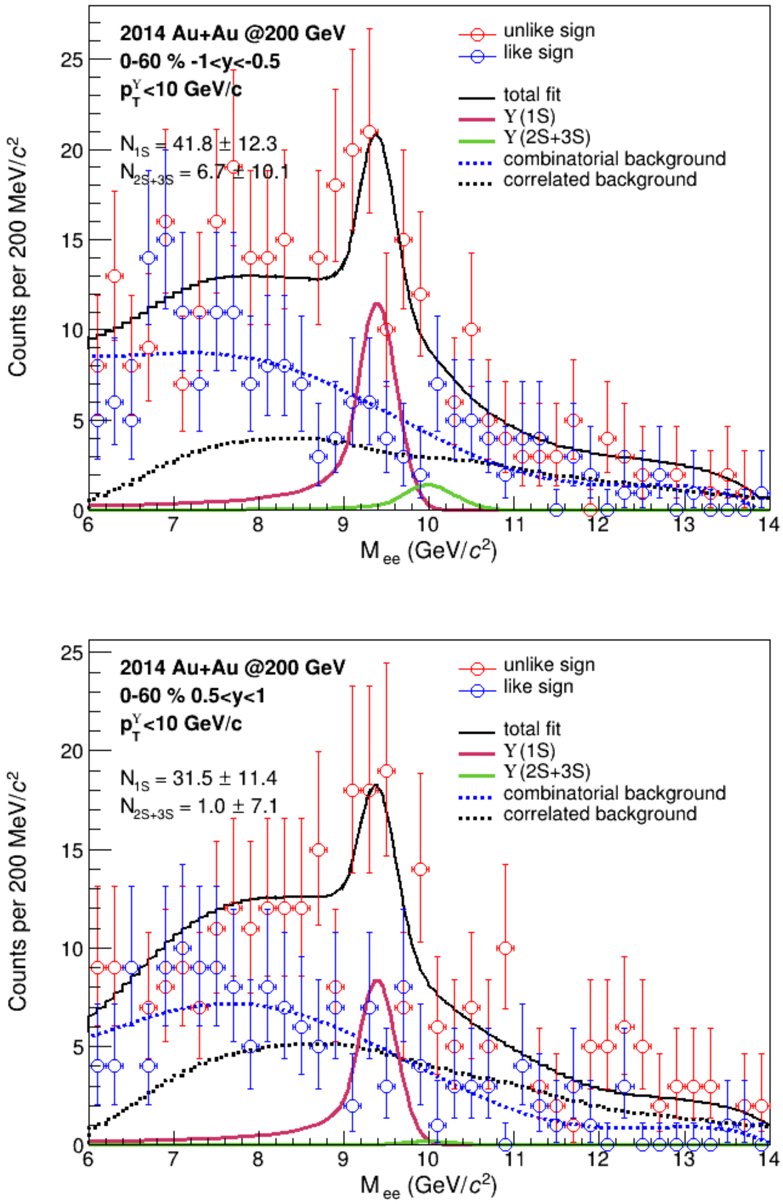

Figure 5.8: THIS ANALYSIS: Reconstructed Υ signal in 0-60% centrality class for $-1 < y < -0.5$ and $0.5 < y < 1$ rapidities.

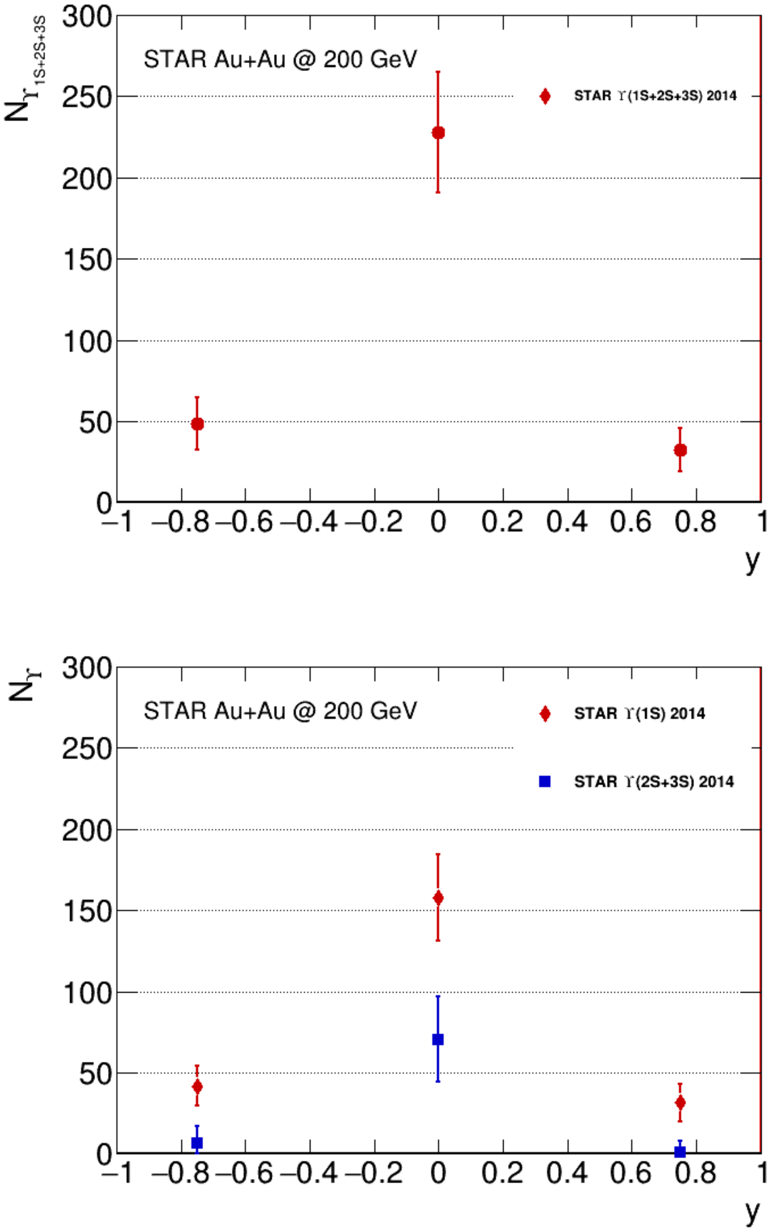

Figure 5.9: THIS ANALYSIS: Υ(1S+2S+3S), Υ(1S) and Υ(2S+3S) yield dependence on rapidity for 0-60% centrality class.

real production. For particle transport simulation and detector geometry description GEANT software has been used. Number of reconstructed particles form Monte Carlo simulation is a priori known. Efficiency is defined as a ratio of reconstructed particles from Monte Carlo and from real data.

Results shown here are processed with old simulation data for P15ic production provided by Oliver Matonoha [57], since embedding for P18ih production is not available yet. Moreover, efficiencies are available only for $|y| < 0.5$, therefore R_{AA} calculation is performed only in $|y| < 0.5$ rapidity interval. Efficiences are shown in Fig. 5.10.

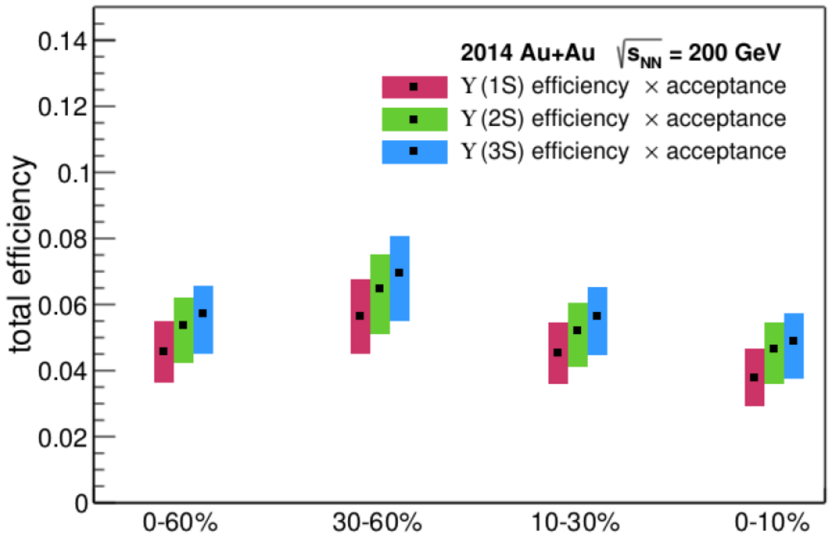

Figure 5.10: Values of the total reconstruction efficiency in different centrality classes for the Υ(1S) (red color), Υ(2S) (green color), and Υ(3S) (blue color) taken from Oliver Matonoha [58].

5.6 Nuclear Modification Factor R_{AA}

In order to be able to compare Υ yield from Au+Au to p+p collisions and compute R_{AA}, invariant Υ yield $\frac{dN_{\Upsilon}^{\text{inv}}}{dp_T dy}$ has to be calculated. Invariant Υ yield is calculated as follows:

$$\frac{dN_{\Upsilon}^{\text{inv}}}{dp_T dy} = \frac{N_{\Upsilon}^{\text{raw}}}{\varepsilon_{\Upsilon} \cdot \int \mathcal{L}dt \cdot \sigma_{\text{Au+Au}}^{\text{inel}} \cdot \Delta_{\text{cent}} \cdot \Delta y} \quad , \tag{5.4}$$

where $N_{\Upsilon}^{\text{raw}}$ is the raw yield of the state, ε_{Υ} its total reconstruction efficiency and acceptance, $\int \mathcal{L}dt$ is integrated luminosity, $\sigma_{\text{Au+Au}}^{\text{inel}} = 6$ b is the total inelastic cross-section of an Au+Au collision at $\sqrt{s_{NN}} = 200$ GeV [61], Δ_{cent} is the fraction of the cross section corresponding to the centrality bin (0-10% $\sim$ 0.1) and Δy is size of rapidity interval.

$$R_{AA} = \frac{\sigma_{\text{p+p}}^{\text{inel}}}{\langle N_{\text{coll}} \rangle} \frac{\frac{dN_{\Upsilon}^{\text{inv}}}{dp_T dy}}{\frac{d\sigma_{\Upsilon}^{\text{pp}}}{dp_T dy}} \tag{5.5}$$

In calculation of R_{AA} in Eq. (5.5), total inelastic cross section of a p+p collision $\sigma_{\text{p+p}}^{\text{inel}} = 42$ mb [61], mean number of binary collisions $\langle N_{\text{coll}} \rangle$ from Glauber model, Υ cross-section in p+p collisions $\frac{d\sigma_{\Upsilon}^{\text{pp}}}{dy} = 81.0 \pm 9.2$ pb [62] and invariant Υ yield $\frac{dN_{\Upsilon}^{\text{inv}}}{dy}$

is used. Results of R_{AA} calculation can be seen in Fig. 5.11. In 0-60% centrality interval and $|y| < 0.5$ rapidity interval $R_{AA} = 0.29 \pm 0.06$ for Υ(1S) and $R_{AA} = 0.25 \pm 0.10$ for Υ(2S+3S) has been obtained. Computation for central collisions lead to $R_{AA} = 0.19 \pm 0.08$ for Υ(1S) and $R_{AA} = 0.41 \pm 0.18$ for Υ(2S+3S).

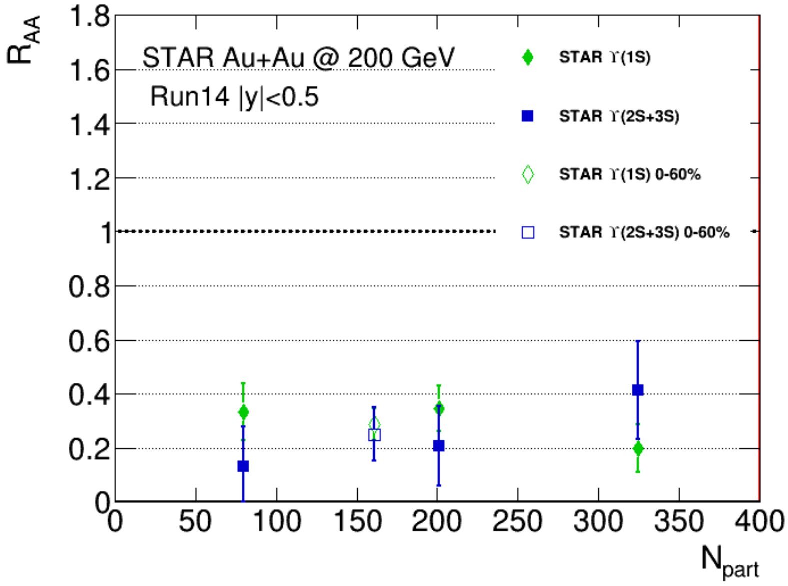

Figure 5.11: THIS ANALYSIS: Calculated dependence of nuclear modification factor R_{AA} on number of participants N_{part}.

5.7 Discussion

In this last section, results of the analysis will be compared with results of former co-worked Oliver Matonoha and with STAR collaboration results from chapter 3, firstly raw yields, secondly R_{AA}. Finally, possible explanations will be given.

Our cut	Oliver Matonoha's cut
DCA$\leq$ 3 cm	DCA$\leq$ 0.75 cm
$-1.3 \leq n\sigma_e \leq 3$	$-1.5 < n\sigma_e < 3$
$0.7 \leq \frac{E_{clu}}{p} \leq 1.4$	$0.75 < \frac{E_{clu}}{p} < 1.5$
$R \leq 0.026$	$R < 0.025$

Table 5.4: Summary of cuts that differ in our analysis and Oliver Matonoha's analysis [5][58].

Since Oliver's analysis of data from Run 2014, bugs in reconstruction algorithms were found and data had to be reproduced, which implies better quality of the new

[5]Cut $nHitsFit \geq 20$ applies in both analyses [57].

data. Results of Υ raw yield calculation performed by Oliver Matonoha are shown in Fig. 5.12 and Fig. 5.13. In Tab. 5.4 cuts, that are different with respect to our analysis, are presented. Numbers of reconstructed Υ(1S) and Υ(2S+3S) are compatible within errors in all centralities, although in 0-10% and 30-60% regions Υ(2S+3S) results differ by a factor of two. After dividing into centrality ranges, most Υ states falls into semi-central one in both cases.

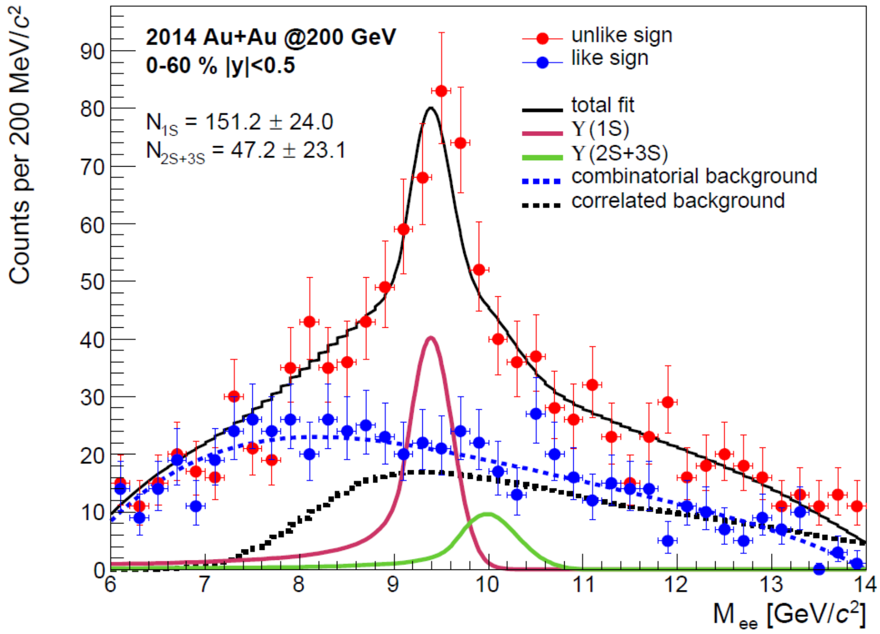

Figure 5.12: Reconstructed Υ signal in 0-60% centrality class by Oliver Matonoha [58].

R_{AA} calculated in this analysis surprisingly does not follow expected shape. In results of CMS and STAR collaborations, mentioned in chapter 3, a trend of bigger suppression with increasing centrality can easily be recognized. In addition, in CMS and STAR results Υ(2S+3S) is suppressed in semi-central and central collisions more than Υ(1S). In our result, Υ(2S+3S) is more suppressed than Υ(1S) only in peripheral and semi-central collisions. However, this trend may not be significant due to large uncertainties. In central collisions, the point for Υ(2S+3S) is observed above the Υ(1S) point within uncertainties. Also, it evinces that suppression of Υ(1S) as well as of Υ(2S+3S) is centrality independent for central and semi-central collisions.

In Fig. 5.14, R_{AA} dependence on N_{part} calculated by Oliver can be seen. In comparison to the result presented in this research project, both Υ(1S) and Υ(2S+3S) agree within error bars. However, except of semi-central an central collisions for Υ(2S+3S), all our data are systematically lower than Oliver's. The biggest difference can be seen in the peripheral region where newly calculated R_{AA} is approximately two times fold lower than that calculated by Oliver or that in STAR results shown in previous chapter. Moreover, in the most central collisions we observe for Υ(1S) suppression $R_{AA} \sim 0.2$, Oliver's result is $R_{AA} \sim 0.35$, while in the latest STAR results $R_{AA} \sim 0.6$ has been observed.

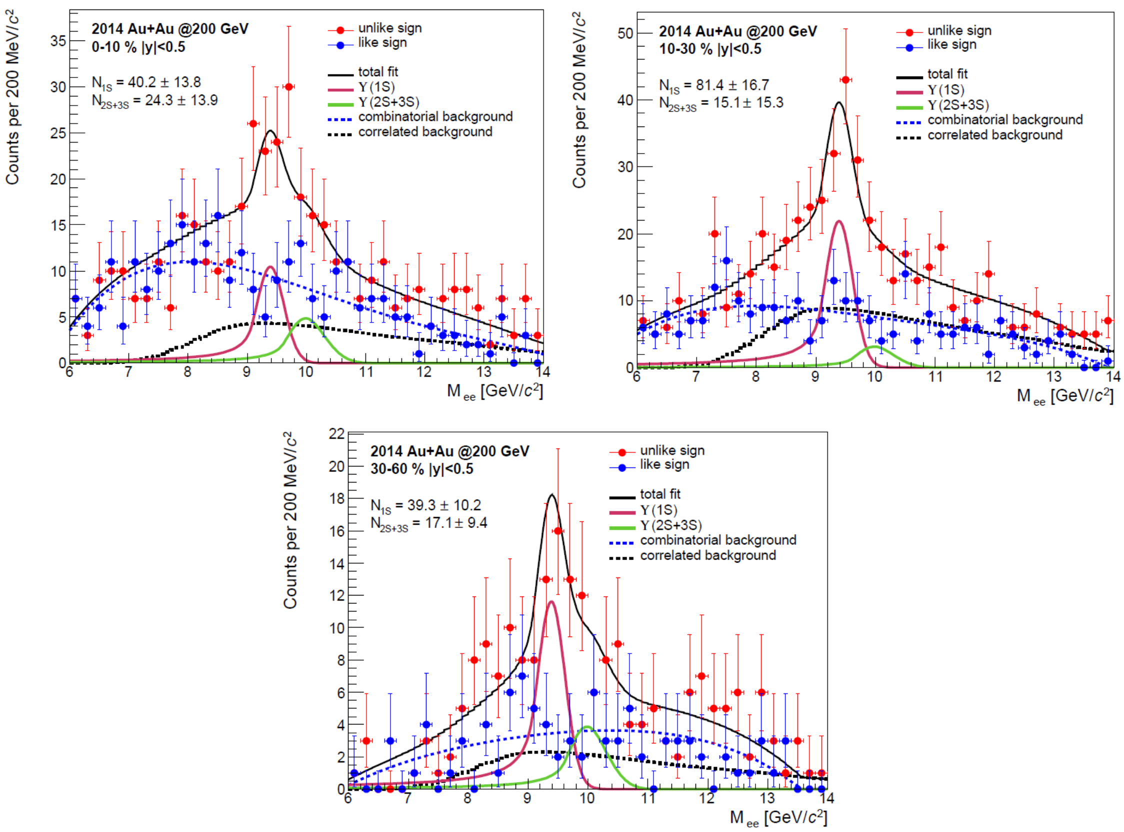

Figure 5.13: Reconstructed Υ signal in 0-10%, 10-30%, 30-60% centrality classes by Oliver Matonoha [58].

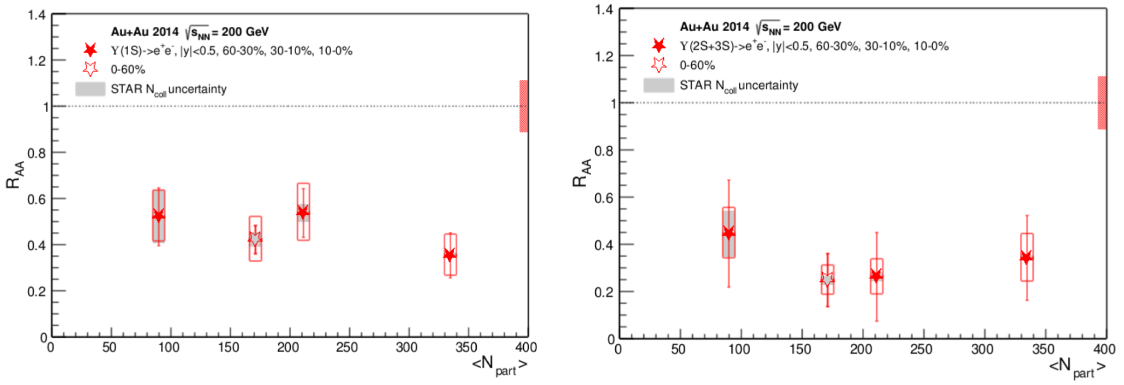

Figure 5.14: Reconstructed nuclear modification factor R_{AA} for Υ(1S) (left) and Υ(2S+3S) (right) by Oliver Matonoha [58].

However, graphs from Oliver's thesis [58], that are showed in Fig. 5.14, are not the latest ones. Oliver did not apply $|\eta| < 1$ cut for electrons in simulation for efficiency calculation [57]. New Oliver's results can be seen in Fig. 5.15 where they are compared with results from this research project. Results totally match.

Possible explanation for different observed production suppression may be implementation of the old simulation data for efficiency calculation that are not up to date. The efficiencies still have to be recalculated for new set of cuts and the new dataset. Next, newly reproduced dataset with fixed tracking bug and different settings in data has been chosen for this analysis. The absence of HFT tracking may resulted in efficiency decrease which causes lower observed signal. Another reason for decrease in R_{AA} is analysis of larger part of dataset than Oliver performed whilst Υ signal remained almost the same.

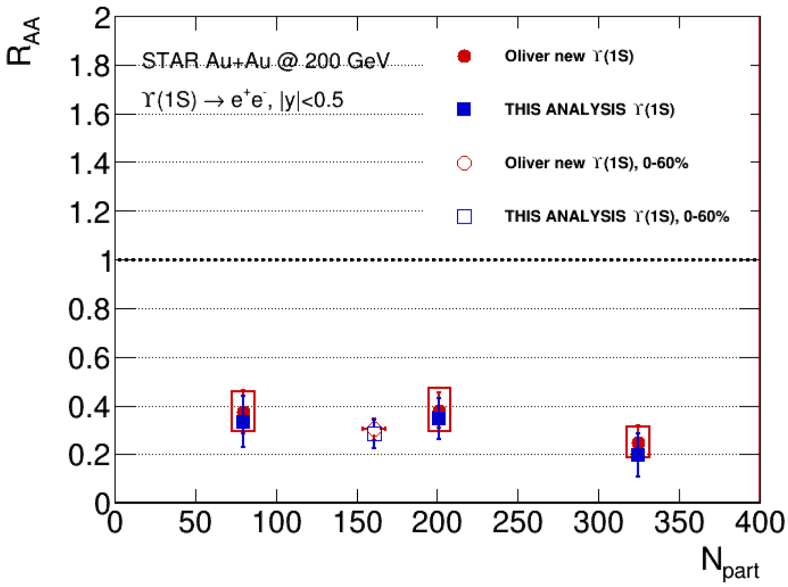

Figure 5.15: Comparison of Υ(1S) Oliver's latest result of R_{AA} dependence on N_{part} [57] with our result. Hollow marker denotes centrality $0 - 60\%$.

Conclusion

For medium with sufficiently high temperature, MIT Bag Model and lattice QCD calculations predict creation of state of matter where quarks and gluons are deconfined and can move freely within the medium. Such state of matter is called quark-gluon plasma (QGP) and is formed in nuclei collision. Many scientists around all of the world currently intensively study various properties of QGP by different methods, e.g. by quarkonium suppression.

Object of the research project is to study Υ production modification in Au+Au collisions at $\sqrt{s_{NN}} = 200$ GeV at STAR. Υ(1S) and Υ(2S+3S) invariant mass spectra have been reconstructed via dielectron channel from Run 14 data in four centrality bins. For signal extraction, combinatorial background has been estimated by like-sign method. Also raw yield rapidity dependence has been shown. To correct yield efficiencies, embedding simulation from old data production have been used. Finally, nuclear modification factor R_{AA} dependence on number of participants N_{part} has been calculated.

From signal extraction $N_{1S} = 157.7 \pm 26.5$ of Υ(1S) and $N_{2S+3S} = 70.3 \pm 26.3$ of Υ(2S+3S) have been reconstructed in rapidity $|y| < 0.5$ and cetrality $0 - 60\%$. It has been found that approximately half of Υ(1S) originates from semi-central collisions while in case of Υ(2S+3S) slightly more than half of reconstructed Upsilons originates from central collisions. Totally $N_{1S+2S+3S} = 228 \pm 37.3$ Υ(1S+2S+3S) has been reconstructed in $0 - 60\%$ centrality interval and $|y| < 0.5$ rapidity interval. Outside of $|y| < 0.5$ interval the lower number of Upsilons has been reconstructed: $N_{1S} = 41.8 \pm 12.3$ and $N_{2S+3S} = 6.7 \pm 10.1$ in $-1 < y < -0.5$ interval and $N_{1S} = 31.5 \pm 11.4$ and $N_{2S+3S} = 1.0 \pm 7.1$ in $0.5 < y < 1$ interval. Values of N_{2S+3S} in both $-1 < y < -0.5$ and $0.5 < y < 1$ rapidity intervals are very small and consistent with no signal. Next, signal rapidity dependence has been obtained.

In R_{AA} dependence on N_{part}, greater suppression in peripheral and semi-central collisions than in central ones has been observed for Υ(2S+3S) while for Υ(1S) lower suppression in peripheral and semi-central than in central collisions can be seen. However, within uncertainties the dependence on N_{part} is not significant. In 0-60% centrality interval and $|y| < 0.5$ rapidity interval R_{AA} has been found to be $R_{AA} = 0.29 \pm 0.06$ for Υ(1S) and $R_{AA} = 0.25 \pm 0.10$ for Υ(2S+3S). Computation for central collisions lead to $R_{AA} = 0.19 \pm 0.08$ for Υ(1S) and $R_{AA} = 0.41 \pm 0.18$ for Υ(2S+3S).

Our results of R_{AA} are significantly smaller than that calculated by Oliver Matonoha in his thesis [58] or by STAR collaboration. However, our data are more consistent with Oliver's latest result [57] which has been calculated with the same new efficiency calculation method. The difference in R_{AA} with respect to STAR results suggests that there may be a potential issue with the efficiency calculation method. Also use of old simulation data or absence of HFT tracking may lead to observed difference. This difference may diminish by applying properly calculated new efficiencies for the new dataset.

Bibliography

[1] Aad, G., Abbott, B., Abdallah, J., Abdel Khalek, S., Abdinov, O., Aben, R., ... Zwalinski, L. (2014). Measurement of the total cross section from elastic scattering in pp collisions at $\sqrt{s} = 7$ TeV with the ATLAS detector. Nuclear Physics B, 889, 486–548. https://doi.org/10.1016/j.nuclphysb.2014.10.019

[2] United-states.cern. The Standard Model and beyond. Retrieved from: http://united-states.cern/physics/standard-model-and-beyond

[3] Petráček, V. Subatomová fyzika I. 2009. Retrieved from: https://physics.fjfi.cvut.cz/files/predmety/02SF/common/subatomovkabook-obr-zc12.2.10.pdf

[4] Mutuk, H. (2019). Cornell Potential: A Neural Network Approach. Advances in High Energy Physics, 2019, 1–9. https://doi.org/10.1155/2019/3105373

[5] Sarkar, S., Satz, H., & Sinha, B. (Eds.). (2010). The Physics of the Quark-Gluon Plasma. Lecture Notes in Physics. Springer Berlin Heidelberg. https://doi.org/10.1007/978-3-642-02286-9

[6] Toia, A. Participants and spectators at the heavy-ion fireball. Retrieved from: http://cerncourier.com/cws/article/cern/53089

[7] Vogt, R. Ultrarelativistic heavy-ion collisions. London: Elsevier, c2007. ISBN 0444521968.

[8] Pasechnik, R., & Šumbera, M. (2017). Phenomenological Review on Quark–Gluon Plasma: Concepts vs. Observations. Universe, 3(1), 7. https://doi.org/10.3390/universe3010007

[9] Wong, C.-Y. (1994). Introduction to High-Energy Heavy-Ion Collisions. WORLD SCIENTIFIC. https://doi.org/10.1142/1128

[10] U. Heinz *et al.*, "Exploring the properties of the phases of QCD matter - research opportunities and priorities for the next decade," arXiv:1501.06477 [nucl-th].

[11] Andronic, A., Arleo, F., Arnaldi, R., Beraudo, A., Bruna, E., Caffarri, D., ... Zhuang, P. (2016). Heavy-flavour and quarkonium production in the LHC era: from proton–proton to heavy-ion collisions. The European Physical Journal C, 76(3). https://doi.org/10.1140/epjc/s10052-015-3819-5

[12] F. Karsch and E. Laermann, Thermodynamics and in-medium hadron properties from lattice QCD, in Quark-Gluon Plasma III, R. C. Hwa and X.-N.Wang, eds. World Scientific Publishing Co. Pte. Ltd., 2004. arXiv:hep-lat/0305025.

[13] T. Matsui and H. Satz, J/Ψ suppression by quark-gluon plasma formation, Phys. Lett. B 178 (1986) 416, doi:10.1016/0370-2693(86)91404-8.

[14] H. Satz, Colour deconfinement and quarkonium binding, J.Phys. G32 (2006) R25, arXiv:hep-ph/0512217 [hep-ph].

[15] Digal, S., Petreczky, P., & Satz, H. (2001). Quarkonium feed-down and sequential suppression. Physical Review D, 64(9). https://doi.org/10.1103/physrevd.64.094015

[16] F. Karsch, D. Kharzeev, and H. Satz, Sequential charmonium dissociation, Phys. Lett. B637 (2006) 75, arXiv:hep-ph/0512239 [hep-ph].

[17] T. Affolder, H. Akimoto, A. Akopian, et al, Production of Υ(1S) Mesons from χ_b Decays in *pbarp* Collisions at s = 1.8 TeV, Phys.Rev.Lett. 84 (2000) 2094-2099, doi:10.1103/PhysRevLett.84.2094.

[18] Du, X., He, M., & Rapp, R. (2017). Color screening and regeneration of bottomonia in high-energy heavy-ion collisions. Physical Review C, 96(5). https://doi.org/10.1103/physrevc.96.054901

[19] Eskola, K. ., Paukkunen, H., & Salgado, C. . (2009). EPS09 — A new generation of NLO and LO nuclear parton distribution functions. Journal of High Energy Physics, 2009(4), 065–065. https://doi.org/10.1088/1126-6708/2009/04/065

[20] Wang, R., Chen, X., & Fu, Q. (2017). Global study of nuclear modifications on parton distribution functions. Nuclear Physics B, 920, 1–19. https://doi.org/10.1016/j.nuclphysb.2017.04.008

[21] Blaizot, J.-P., Gelis, F., & Venugopalan, R. (2004). High energy pA collisions in the color glass condensate approach I: gluon production and the Cronin effect. Nuclear Physics A, 743(1–3), 13–56. https://doi.org/10.1016/j.nuclphysa.2004.07.005

[22] Rezaeian, A. H., & Lu, Z. (2009). Cronin effect for protons and pions in high-energy pA collisions. Nuclear Physics A, 826(1–2), 198–210. https://doi.org/10.1016/j.nuclphysa.2009.05.073

[23] Vogt, R. Cold Nuclear Matter Efects on Open and Hidden Heavy Flavor Production at the LHC. Proceedings, 7th International Workshop on Charm Physics, CHARM 2015: Detroit, USA, May 18-22, 2015. Retrieved from https://inspirehep.net/record/1386865/files/arXiv:1508.01286.pdf

[24] Khachatryan, V., Sirunyan, A. M., Tumasyan, A., Adam, W., Asilar, E., … Woods, N. (2017). Charged-particle nuclear modification factors in PbPb and pPb collisions at $\sqrt{s_{\mathrm{N\,N}}} = 5.02$ TeV. Journal of High Energy Physics, 2017(4). https://doi.org/10.1007/jhep04(2017)039

[25] Bodwin, G. T., Braaten, E., & Lee, J. (2005). Comparison of the color-evaporation model and the nonrelativistic QCD factorization approach in charmonium production. Physical Review D, 72(1). https://doi.org/10.1103/physrevd.72.014004

[26] Krämer, M. (1996). Color-singlet and color-octet contributions to photoproduction. Nuclear Physics B - Proceedings Supplements, 51(3), 195–200. https://doi.org/10.1016/s0920-5632(96)90025-0

[27] ALICE collaboration. (2018) Preliminary Physics Summary: Inclusive Υ production in p-Pb collisions at $\sqrt{s_{NN}} = 8.16$ TeV. Retrieved from: http://cds.cern.ch/record/2317189?ln=pl

[28] Eskola, K. J., Paukkunen, H., & Salgado, C. A. (2009). EPS09 – Global NLO Analysis of Nuclear PDFs and Their Uncertainties. Nuclear Physics A, 830(1–4), 599c–602c. https://doi.org/10.1016/j.nuclphysa.2009.10.054

[29] Acharya, S., Acosta, F. T., Adamová, D., Adolfsson, J., Aggarwal, M. M., Aglieri Rinella, G., ... Zou, S. (2019). Υ suppression at forward rapidity in Pb–Pb collisions at $\sqrt{s_{NN}} = 5.02$ TeV. Physics Letters B, 790, 89–101. https://doi.org/10.1016/j.physletb.2018.11.067

[30] Du, X., He, M., & Rapp, R. (2017). Color screening and regeneration of bottomonia in high-energy heavy-ion collisions. Physical Review C, 96(5). https://doi.org/10.1103/physrevc.96.054901

[31] Krouppa, B., Rothkopf, A., & Strickland, M. (2018). Bottomonium suppression using a lattice QCD vetted potential. Physical Review D, 97(1). https://doi.org/10.1103/physrevd.97.016017

[32] López, J. (2018, May) Quarkonia production in small and large systems measured by ATLAS. Talk session presented at the Quark Matter 2018. Retrieved from: https://indico.cern.ch/event/656452/contributions/2870012/attachments/1648418/2635683/Lopez_QM2018_Talk.pdf

[33] Tuli, S. (2018, May) Probing QCD deconfinement with sequential quarkonium suppression of three Υ(nS) states with the CMS detector. Talk session presented at the Quark Matter 2018. Retrieved from https://indico.cern.ch/event/656452/contributions/2870010/attachments/1649412/2637763/QM18_SantonaTuli.pdf

[34] Wang, P. (2018, May) Υ measurements in Au+Au collisions at $\sqrt{s_{NN}} = 200$ GeV with the STAR experiment. Talk session presented at the Quark Matter 2018. Retrieved from https://indico.cern.ch/event/656452/contributions/2870011/attachments/1649058/2636575/Upsilon_draft_QM2018v13.pdf

[35] Accelerator Division (2006, Nov.) RHIC Configuration Manual. Retrieved from https://www.bnl.gov/cad/accelerator/docs/pdf/RHICConfManual.pdf

[36] Tannenbaum, M. J. (2014). Highlights from BNL-RHIC. In What We Would Like LHC to Give Us. WORLD SCIENTIFIC. https://doi.org/10.1142/9789814603904_0022

[37] Brookhaven National Laboratory (2019, June 13) Run overview of the Relativistic Heavy Ion Collider. Retrieved from http://www.rhichome.bnl.gov/RHIC/Runs/

[38] Campbell, S. (2017). sPHENIX: The next generation heavy ion detector at RHIC. Journal of Physics: Conference Series, 832, 12012. https://doi.org/10.1088/1742-6596/832/1/012012

[39] Brookhaven National Laboratory, STAR Future & Upgrade. Retrieved from https://drupal.star.bnl.gov/STAR/book/export/html/7410

[40] Anderson, M., Berkovitz, J., Betts, W., Bossingham, R., Bieser, F., Brown, R., ... Zhang, W. (2003). The STAR time projection chamber: a unique tool for studying high multiplicity events at RHIC. Nuclear Instruments and Methods in Physics Research Section A: Accelerators, Spectrometers, Detectors and Associated Equipment, 499(2–3), 659–678. https://doi.org/10.1016/s0168-9002(02)01964-2

[41] Bichsel, H. Comparison of Bethe-Bloch and Bichsel Functions, 2002. Retrieved from http://lhcb-vd.web.cern.ch/lhcb-vd/html/Assembly/Reference/sensors/silicondedx/sn0439.pdf

[42] M. Beddo,et al.,The STAR barrel electromagnetic calorimeter, Nuclear Instruments andMethods in Physics Research, Section A: Accelerators, Spectrometers, Detectors andAssociated Equipment, vol. 499, no. 2-3, pp. 725–739, 2003

[43] Brookhaven National Laboratory (2014, June 6) SketchUp STAR. Retrieved from https://drupal.star.bnl.gov/STAR/public/img/SketchUpSTAR

[44] L. Ruan et al, J. Phys G36(2009), 095001.

[45] Yang, C., Huang, X. J., Du, C. M., Huang, B. C., Ahammed, Z., Banerjee, A., ... Zhu, X. L. (2014). Calibration and performance of the STAR Muon Telescope Detector using cosmic rays. Nuclear Instruments and Methods in Physics Research Section A: Accelerators, Spectrometers, Detectors and Associated Equipment, 762, 1–6. https://doi.org/10.1016/j.nima.2014.05.075

[46] Brookhaven national laboratory. MTD plots, pictures and photos. Retrieved from: https://drupal.star.bnl.gov/STAR/subsys/mtd/plots-pictures

[47] Llope, W. ., Geurts, F., Mitchell, J. ., Liu, Z., Adams, N., Eppley, G., ... Zhang, W.-M. (2004). The TOFp/pVPD time-of-flight system for STAR. Nuclear Instruments and Methods in Physics Research Section A: Accelerators, Spectrometers, Detectors and Associated Equipment, 522(3), 252–273. https://doi.org/10.1016/j.nima.2003.11.414

[48] Kiryluk, J. (2005). Local Polarimetry For Proton Beams With The Star Beam Beam Counters. In Spin 2004. World Scientific. https://doi.org/10.1142/9789812701909_0152

[49] Xu, Z., Chen, Y., Kleinfelder, S., Koohi, A., Li, S., Huang, H., ... Kotov, I. (2005). A Heavy Flavor Tracker for STAR. Office of Scientific and Technical Information (OSTI). https://doi.org/10.2172/887418

[50] Contin, G. (2016). The STAR Heavy Flavor Tracker and Upgrade Plan. Nuclear Physics A, 956, 858–861. https://doi.org/10.1016/j.nuclphysa.2016.02.064

[51] C. E. Allgower,et al.,The STAR endcap electromagnetic calorimeter, Nuclear Instru-ments and Methods in Physics Research, Section A: Accelerators, Spectrometers, Detec-tors and Associated Equipment, vol. 499, no. 2-3, pp. 740–750, 2003

[52] STAR TOF Collaboration, Proposal for a Large Area Time of Flight System for STAR, Science And Technology, 2003.

[53] ROOT Data Analysis framework, https://root.cern.ch/

[54] C. Amsleret et al.(Particle Data Group), PL B667, 1 (2008) and 2009 partial update for the 2010 edition. Retrieved from http://pdg.lbl.gov

[55] Bichsel, H. (2006). A method to improve tracking and particle identification in TPCs and silicon detectors. Nuclear Instruments and Methods in Physics Research Section A: Accelerators, Spectrometers, Detectors and Associated Equipment, 562(1), 154–197. https://doi.org/10.1016/j.nima.2006.03.009

[56] Gavin, S., McGaughey, P. L., Ruuskanen, P. V., & Vogt, R. (1996). Lepton production from charm decay in nuclear collisions at $\sqrt{s} = 200$ GeV and 5.5 TeV per nucleon. Physical Review C, 54(5), 2606–2623. https://doi.org/10.1103/physrevc.54.2606

[57] Oliver Matonoha - private conversation, oliver.matonoha@gmail.com

[58] Matonoha, O. (2018). Upsilon meson production in heavy-ion collisions at the STAR experiment, Master's thesis at Czech Technical University in Prague

[59] J. E. Gaiser, Charmonium Spectroscopy From Radiative Decays of the J/ψ and ψ', pp. SLAC–R–0255, http://inspirehep.net/record/183554, 1982.

[60] Zha, W., Yang, C., Huang, B., Ruan, L., Yang, S., Tang, Z., & Xu, Z. (2013). Systematic study of the experimental measurements on ratios of different Υ states. Physical Review C, 88(6). https://doi.org/10.1103/physrevc.88.067901

[61] Adamczyk, L., Adkins, J. K., Agakishiev, G., Aggarwal, M. M., Ahammed, Z., Alekseev, I., ... Zyzak, M. (2014). Suppression of Υ production in d+Au and Au+Au collisions at $\sqrt{s_{NN}} = 200$ GeV. Physics Letters B, 735, 127–137. https://doi.org/10.1016/j.physletb.2014.06.028

[62] Matonoha, O. (2017). Measurements of the Υ meson production in Au+Au collisions at the STAR experiment. Proceedings of Science. Vol. EPS-HEP2017.